UNIVERSITY OF GDAŃSK
Faculty of Chemistry
ul. Wita Stwosza 63
80-308 Gdańsk, Poland

Selvaraj Sengottiyan

„From organic molecules to the nanoscale: The computational framework to design and improve functional materials”

PhD Thesis

Supervisor:
Prof. dr hab. Tomasz Puzyn
Co-supervisor:
Dr. Alicja Mikołajczyk

Gdańsk 2023

TABLE OF CONTENTS

ACKNOWLEDGEMENTS

First, I would like to express my sincere gratitude to my thesis advisor, Prof. Tomasz Puzyn, and my co-supervisor, Dr. Alicja Mikołajczyk, for allowing me to conduct this study. I thank my supervisors for their guidance and advice, which allowed me to complete all phases of the written development of my project. I thank the members of my committee for their advice, which will be useful to me in my doctoral defense, and for their insightful comments and suggestions.

My dissertation would have been impossible without the cooperation of Dr. Karolina Jagiełło, Dr. Agnieszka Gajewicz-Skrętna, Marta Swirog, Michał Kałapus, and Sattibabu. I thank Katarzyna Dembowska and Martyna Urbanowicz for their support throughout the process.

Next, I would also like to thank them for their financial support. All my research was supported by the Horizon 2020 research and innovation programme of the European Union under the NanoInformaTIX project under grant agreement No. 814426 and the DIAGONAL project No. 953152.

Also, I would like to thank my wife Suganya Selvaraj, and my entire family for their unwavering support and tolerance in conducting my research and writing my project. I thank you for your prayers that I have come this far.

Finally, I would like to thank God for guiding me through all the challenges. I have felt your guidance every day. Thanks to you, I was able to complete my studies. I will continue to put my trust in you in the future.

ABBREVIATIONS

CO	Carbon-monoxide
PYD	Pyrene derivative
PS1	N '-pyrene-1-ylmethylene-hydrazine-carbodithioic acid methyl ester
PS2	N' -pyrene-1-ylmethylene-hydrazine-carbodithioic acid benzyl ester
SBDTC	S-benzyl dithiocarbazate-based Schiff-bases
SB	Schiff-based
MDRB	Multi-Drug Resistance Bacteria
MIC	Minimal inhibitory concentration
KB-1	4-[(pyren-1-ylmethylene) amino] phenol
MRSA	Methicillin-Resistant Staphylococcus Aureus
HOMO	Highest Occupied Molecular Orbital
LUMO	Lowest Unoccupied Molecular Orbital
BSA	Bovine serum albumin
HAS	Human serum albumin
CN^-	Cyanide anion
WHO	World health organization
μM	Micromolar
DMSO/EtOH	Dimethyl sulfoxide/Ethanol
S29	1,4-2,2-dicyanovinyl benzene
S31	2-(4-(bis(4-(5-methyl-2,4-dioxo-3,4-dihydropyridine-1-(2H)-yl)-oxy) phenyl) amino) benzylidene-malononitrile
DMN	(2-[[7-[5-[bis(4-methylphenyl)-amino]-2-thienyl]-2,1,3-benzothiadiazol-4-yl] methylene] propane nitrile)
ICT	Intramolecular charge transfer
BT	2,1,3-benzothiadiazole
QM	Quantum mechanics
TD-DFT	Time-Dependent Density Functional Theory
PNPs	Polymer nanoparticles
NP	Nanoparticle
Nano-QSPR	nano - Quantitative Structure-Property Relationship
GA-PLS	Genetic Algorithm-Partial least square
Q^2_{EXT}	External predictive
PLGA	Poly (lactic-co-glycolic acid)
PEG	Polyethylene glycol
RMSEC	Root-mean-square error calibration
RMSECv	Root-mean-square error cross-validation
MTX-SS-γ-PGA	Methotrexate-disulfide-hydrophilic γ-polyglutamic acid
EPR	Enhanced Permeability and Retention
DDS	Drug Delivery System
PGA	Polyglutamic acid

MESP	Molecular electrostatic potential
PC	Protein corona
FP	Fingerprint
Q^2_{cv}	Cross-validated (leave-one-out) correlation coefficient
$RMSE_P$	Root-mean-square error prediction
R^2	Determination coefficient
Q^2	Correlation coefficient

RESEARCH PAPERS SUBMITTED AS PhD THESIS

[A] **Selvaraj Sengottiyan,** Kakoli Malakar, Arunkumar Kathiravan, Marappan Velusamy, Alicja Mikolajczyk, and Tomasz Puzyn. Integrated Approach to Interaction Studies of Pyrene Derivatives with Bovine Serum Albumin: Insights from Theory and Experiment. *J. Phys. Chem. B* 2022, 126, 3831−3843. [IF 2021 = 3.466; MNiSW 2022 =140]; doi.org/10.1021/acs.jpcb.2c00778

[B] **Selvaraj Sengottiyan,** Alicja Mikolajczyk, Tomasz Puzyn. How does the study MD of pH-dependent exposure of nanoparticles affect cellular uptake of anticancer drugs? *Int. J. Mol. Sci.* 2023, Published on-line [IF 2022 = 6.208; MNiSW 2022 =140];

[C] **Selvaraj Sengottiyan,** Alicja Mikolajczyk, Karolina Jagiełło, Marta Swirog, and Tomasz Puzyn. Core, coating, or corona? The importance of considering protein coronas in nano-QSPR modeling of zeta potential. *ACS Nano* 2023, Published on-line [IF 2022 = 18.027; MNiSW 2022 =200]; doi.org/10.1021/acsnano.2c06977

[D] Arunkumar Kathiravan, **Selvaraj Sengottiyan,** Tomasz Puzyn, Pushparathinam Gopinath, Kanagachidambaresan Ramasubramanian, Praveen Ayyappan Susila, and Mariadoss Asha Jhonsi. Rapid colorimetric discrimination of cyanide ions–mechanistic insights and applications. *Anal. Methods* 2022, 14, 518-525. [IF 2022 = 3.532; MNiSW 2022 =70]; doi.org/10.1039/D1AY02040D

Total impact factor: 31.233

Total MNiSW points: 550

OTHER PUBLICATIONS

[E] **Selvaraj Sengottiyan,** and Selvan Nehru. Integrating electronic properties of Prodan by parameterization: Combining theory with experimentation. *J. Mol. Struct.* 2021, 1241, 130639. [IF 2022 = 3.841; MNiSW 2022 =70];

[F] Okoli, Chuka, **Selvaraj Sengottaiyan,** N. Arul Murugan, Asalapuram R. Pavankumar, Hans Ågren, and Gunaratna Kuttuva Rajarao. In silico modeling and experimental evidence of coagulant protein interaction with precursors for nanoparticle functionalization. *J. Biomol. Struct. Dyn.* 2013, 31, 1182-1190. [IF 2021 = 5.235; MNiSW 2021 =70];

[G] **Selvaraj Sengottiyan,** N. Arul Murugan, and H. Ågren. Al^{3+} induced planarization, conformational arrest and metallochromic shift in a pyrimidine dione dye: insight from integrated hybrid quantum–classical calculations. *PCCP.* 2012, 14, 2339-2345. [IF 2022 = 3.945; MNiSW 2022 =100];

[H] Jhonsi, M. Asha, **S. Selvaraj,** G. Paramaguru, P. Venuvanalingam, and R. Renganathan. Spectroscopic and molecular docking investigations on the interaction of rutin with bovine serum albumin. *Zeitschrift für Physikalische Chemie.* 2011, 225, 441-454. [IF 2022 = 4.315; MNiSW =70];

[I] Paramaguru, G., A. Kathiravan, **S. Selvaraj,** P. Venuvanalingam, and R. Renganathan. Interaction of anthraquinone dyes with lysozyme: evidences from spectroscopic and docking studies. *J. Hazard. Mater.* 2010, 175, 985-991. [IF 2022 = 14.224; MNiSW 2022 =200];

Total impact factor: 31.560

Total MNiSW points: 510

SUMMARY OF THE RESEARCH CONDUCTED

The future of the European industry requires advances in the development and characterization of advanced chemicals and organic compound chemicals in combination with nanoforms of the substance, leading to the reliable development of new, safe, and sustainable chemicals for various applications, such as antibacterial activity and efficient drug delivery. The development of new, advanced chemicals requires an understanding of the relationship between their structure, physicochemical properties, and the potential hazards that newly developed chemicals may pose to humans and the environment. Unfortunately, experimental studies using various complex methods are time-consuming and costly. Several strategies have been proposed in the literature to reduce the number of experiments and increase the efficiency of selecting an 'optimal candidate'. One of the most promising approaches for the development of new functional chemicals is based on a computational framework combined with experimental validation. For example, pyrene derivatives developed from functionalized Schiff-based compounds are useful measures against bacterial infections and therefore have the potential to be used as effective drugs against multidrug-resistant bacteria (MDR). However, to date, binding studies with plasma proteins, such as bovine serum albumin (BSA), are still unknown; thus, a better understanding of the binding mechanism in truly drug-based applications is still limited. Therefore, in the first case study **[A]**, I proposed an integrated approach based on molecular dynamics (MD) and experimental validation to investigate the interaction and stability of BSA with newly synthesized potent pyrene derivatives (PS1 and PS2). In addition, Poisson-Boltzmann molecular surface mechanics (MMPBSA) with Gromacs software were used to determine the free energies of binding BSA-PS1 and BSA-PS2 complexes at 300 K. The results obtained based on MD may be crucial for the efficient design of new functionalized Schiff-based pyrene derivatives in a virtual (computational) space. The efficacy of new drugs can be enhanced by functionalizing and coupling organic molecules with the nanoforms of the substance (NPs). However, there is limited knowledge about the uptake of newly developed NP-based drug delivery systems by biological cells; thus, because of this lack, many drugs fail in the first phase of clinical trials. Therefore, in the second case study **[B]**, I applied MD to investigate the influence of the selected physicochemical properties of the cancer drug methotrexate (MTX) grafted with hydrophilic-γ-polyglutamic acid (MTX-SS-γ-PGA) on its cellular uptake at different pH values. For this study, three theoretical models describe drug-loaded nanoparticles (MTX-SS-γ-PGA) at three different pH values, such as (1)

pH 7.0 (the so-called neutral pH model), (2) pH 6.4 (the so-called tumor pH model), and (3) pH 2.0 (the so-called stomach pH model). The cellular uptake mechanism was proposed by free energy barrier analysis using classical MD and MD-based umbrella sampling methods supported by the WHAM tool. The proposed research reveals fundamental insights into molecular dynamics that will allow researchers to determine the influence of the pH, structure, charge, and energy of NPs on the cellular uptake of anticancer drugs. The presented study may be a starting point for the efficient and safe development of models critical for drug delivery to cancer cells at the earliest possible stage (before humans). However, it should be kept in mind that many other factors may influence the uptake of nanoparticles, including the physicochemical properties of nanoparticles, protein–particle interactions, and subsequent agglomeration, diffusion, and sedimentation. Accordingly, NPs can agglomerate rapidly in response to changes in the dispersing environment and form particles with large diameters. Depending on biological conditions (especially pH), the agglomerate can dissociate and become a source of much smaller (often more toxic) particles in the body, such as a "Trojan horse." The agglomerate formation is strongly dependent on surface charge (zeta potential (ζ)), which stabilizes dispersed nanoparticles and prevents their agglomeration. Therefore, to control stability in a biological medium, several factors affecting the zeta potential (ζ) of nanoparticles (NPs) must be considered, including complex interactions between the nanostructure and the composition of the protein corona (PC). Effective *in silico* methods (based on machine learning and quantitative structure-property relationships (QSPRs)) could help predict and characterize the relationship between the physicochemical properties of NP and the formation of PC and biological outcomes in the medium at an early stage of experimentation. However, currently developed models are limited to simple descriptors that do not represent the complex interactions between the core, the coating, and their PC fingerprints. In this context, in the third case study **[C]**, for the first time, a set of complex descriptors was developed that describes the quantitative relationship between the value of the zeta potential (ζ), the core, the coating of NPs, and their PC fingerprints (the so-called nano-QSPR model). The nano-QSPR model was developed by partial least squares regression using a genetic algorithm (GA-PLS) and is characterized by a high external predictive power $Q^2_{EXT} = 0.89$.

In addition, the zeta potential can potentially be used as a pre-indicator of cellular interactions with charged ions or NP molecules. When a more positive zeta potential (ζ) (surface charge)

of NPs is present in a biological medium, cellular uptake is likely due to the presence of negatively charged ions in the top layer of the cell membrane. Unfortunately, an excess amount of toxic ions may have unknown toxic effects on the human body and the environment. Therefore, their potential exposure should be controlled in the early stages of new chemical development. To assist this similar kind of process, in the fourth case study **[D]**, I combined TD-DFT calculations with experimental data and used an additional molecular electrostatic potential (MESP) map to understand the mechanism of charge variation in the nucleophilic addition of cyanide ions inside and outside the surface. When cyanide ions enter the bloodstream, they immediately damage the mitochondrial electron transport chain, preventing cells from breathing and interrupting the cellular respiration process. Therefore, the elimination of these toxic ions is a major challenge in the development of new structures. In this context, computational and spectroscopic methods for the intermolecular interaction of the malononitrile-functionalized DMN probe with cyanide ions in solutions are investigated. In this case, a TD-DFT calculation was used to calculate the absorption spectra for these functionalized probes, and our results correlated well with the experimental data. Based on the results obtained, I have described how the colorimetric response of the transition to the malononitrile-functionalized DMN probe prevents intramolecular charge transfer when cyanide ions are added, leading to the development of a Michael channel at the site where the dicyanovinyl group undergoes β-conjugation with cyanide.

Four lessons can be drawn from the thesis presented in the context of the computational design process of safe, sustainable, and targeted chemicals and nanoforms of substances. First, it was directed toward nanoinformaticians. The zeta potential (ζ) of NPs cannot be modeled based on the structure of the NPs themselves. The developed models should be described as functions of both the structural properties determined by the NP core and coating and the biological medium determined by the formation of the protein corona. This will enable reliable predictions for advanced nanosystems for targeted delivery. Second, the project addresses the nanosafety community. The NP protein corona fingerprints (NP features in real-time) could be much more crucial for controlling and governing the zeta potential of NPs than the nanostructure features themselves. Therefore, the change in the fate or uptake of nanosystems due to the formation of a protein corona in the biological medium cannot be ignored. Third, the charge, geometry, and energetics of NP, which affect the cellular uptake mechanism, should be studied by molecular models that describe different and real environments that can be

expressed by different pH values. Fourth, the same newly developed substances that open new opportunities for the industry may pose a serious risk to humans and the natural environment. Therefore, it is critical to evaluate the potential risk of chemical substances that may be present both in the environment (i.e., the human body) and in the aquatic environment.

1. Introduction

1.1. From organic molecules to nanoscale compounds

Organic molecules are generally defined as carbon-containing molecules, with a few exceptions, such as CO[1]. The potential of carbon atoms to form compounds with each other and with other atoms allows a variety of precipitated chemical groups to be joined by larger molecules, including polymers. Decades of research in organic chemistry have yielded insights into many different molecules that can be used to design new functional properties of molecules by integrating different chemical substituents and appending different types of groups that can serve as building blocks for combined functionalities[2]. The ability to create a self-assembly model would allow the design of molecules that would enable the construction of nanostructures and large-scale orders. Although organic molecules are the basis of life, modern chemistry considers a greater variety of molecules than nature[3]. Therefore, in the real world, they can be compatible with biomolecules and combined with proteins and various biomolecules. This finding makes it possible to use the natural ability of many biomolecules to self-assemble and modify the structural arrangement of biomolecules to study different functionalities and design hybrid molecules for many different medical applications. Organic molecules have become more attractive as materials for many applications that previously occurred in nature in many forms, enabling many applications that were not previously available. Organic molecules act as versatile and finely tuned building blocks for specific properties in nanoscale and bulk solids. Based on this aspect, organic compounds are characterized by functional groups that alter the physicochemical properties of the compounds, leading to many potential applications in many fields and industrial sectors, such as medicine, pharmaceuticals, drugs, food, fuels, etc[4]. The field of pharmaceuticals in nanomedicine and nanotechnology is growing rapidly today. Recently, NP consideration has been the most advanced, either in the field of scientific research or in the commercial sector. The size of NPs plays an important role in their physiological and biochemical properties and their different arrangements, such as polymer NPs, fullerenes, metal NPs, and ceramic NPs. They have unique physicochemical properties due to their surface and size, and their physical and chemical properties can differ significantly from those of their larger counterparts[5]. The functional coating improves the physicochemical properties and properties of nanoparticles/nanomaterials for potential applications that play an important role in medicine. It is also believed that

improved performance and adaptability can be achieved through nanoscale modifications and changes in composition, whereby specific potential applications can be achieved. However, in the case of the design of functional groups and/or materials, another difficult task is to align their specific properties and functionalities by developing and applying a specific independent methodology for collecting all information at the atomic level using various complementary techniques. This is called the long-recognized goal of complex modeling[6] and the selection of specific functional groups with specific properties. Functional materials are groups of atoms that are used to develop advanced materials and synthesize them for specific functions with the right structural and morphological arrangements to obtain custom properties for specific applications. Functional materials can therefore have unique physicochemical properties compared to those of simple components. In this context, the migration of organic molecules into the nanoscale allows us to better understand the mechanisms of the behavior of molecules in their environment that shed light on specific applications. Based on this aspect, my dissertation focuses mainly on the industrial application of these specific properties, which implies the development of new functional materials with micro-/nanostructures of compounds using different calculation methods. In this context, organic compounds are characterized by functional groups arranged in a particular group of atoms or molecules, determining certain specific properties that are applied massively to the daily life of humans. For example, pyrene derivatives have been used in a wide range of applications, taking advantage of the unique structural, optical, and charge-transfer properties of pyrene compounds. Polycyclic aromatic hydrocarbon pyrene is a rigid, flat, and planar molecule with unique specific properties due to its structural arrangement, and it is used in many applications. The molecular structure of pyrene is shown in Figure 1.

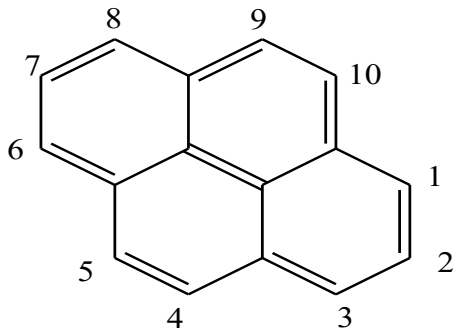

Figure 1. The molecular structure of pyrene has numbered C–H bonds.

Pyrene derivatives are used in many fields, such as organic electronics, bioimaging techniques for fluorescent labels and sensors, confirmatory assembly studies of macromolecules, micelles, and supramolecules, and various applications of the functional groups of pyrene compounds that determine chemical reactivity. In recent decades, Schiff bases have become a category of widely used organic compounds with numerous applications in daily life. In addition to these diverse applications, modifications of Schiff bases[7-10] by condensation of S-substituted dithiocarbazates with various aldehydes and ketones have recently become possible, with considerable attention paid to combating bacterial infections. In contrast, multidrug resistance (MDR) is currently one of the main problems in the treatment of bacterial infections, as the number of MDR bacteria resistant to antibacterial drugs is constantly increasing, leading to a higher probability of treatment failure. In this context, a new drug with new active ingredients with improved efficacy is urgently needed to combat the MDR problem. Based on this need, Hassan et al. (2019)[11] showed, for example, that Schiff-based (SB) functionalized compounds of 5-(benzylideneamino)-3-(4-methoxyphenylamino)-N-phenyl-1H-pyrazole-4-carboxamide outperform ciprofloxacin at minimal inhibitory concentrations (MIC) and are effective against multidrug-resistant bacteria (MDRB). Following Guemues et al. (2020)[12], the compounds were synthesized from SB derivatives with two different basic units, such as anthracene and pyrene units, and their antibacterial activity against Gram-negative Bacillus cereus, Pseudomonas aeruginosa, and E. coli was investigated. Similarly, two SBs, such as 4-(((8-hydroxyquinolin-2-yl)methylene)amino)-1,5-dimethyl-2-phenyl-1,2-dihydro-3H-pyrazol-3-one and 4-(((10-chloroanthracen-9-yl)methylene)amino)-1,5-dimethyl-2-phenyl-1,2-dihydro-3H-pyrazol-3-one were synthesized by Erturk et al. (2020)[13] and exhibited higher antibacterial activity against S. aureus. Mishra et al. (2020)[14] synthesized two SB ligands with benzothiazole derivatives tested against S. aureus, causing skin infections, food poisoning, and pimple-causing bacteria from propionicum acnes. This SB ligand has more antibacterial properties than free SB compounds. Subsequently, Srinivasan et al. (2021)[15] described the synthesis and evaluation of two SBs based on pyrene, such as 4-[(5-pyren-1-yl-thiophen-2-ylmethylene)-amino]-phenol and 4-[(4-pyren-1-yl-benzylidene)-amino]-phenol, which is active against two different types of bacterial strains. Prasad et al. (2022)[16] recently described SB-functionalized piperazine compounds with excellent activity against methicillin-resistant Staphylococcus aureus (MRSA) bacteria, validated by experimental and *in silico* modeling methods. Based on the above importance of SB-

functionalized compounds, pyrene-based SB-functionalized compounds of KB-1 (4-[(pyren-1-ylmethylene) amino] phenol) were synthesized in a report[17] and validated with theoretical DFT studies, indicating that the versatile applications have both antibacterial (Gram (+) and Gram (-)) and antifungal properties; thus, the KB-1 compound acts as an excellent antimicrobial agent and photolabeling agent. However, the above studies on the binding of compounds to proteins are limited, and the mechanism of binding is still unknown. Therefore, our goal is to solve this problem by developing compounds that are more antibacterial than existing ones, which is the main challenge. In this context, the Schiff base functionalized pyrene derivatives PS1 (N'-pyrene-1-ylmethylene-hydrazine-carbodithioic acid methyl ester) and PS2 (N'-pyrene-1-ylmethylene-hydrazine-carbodithioic acid benzyl ester) have been developed and studied with BSA protein using our various computational methods, which are supported by experimental methods and can help improve their antibacterial properties and applications. To address this problem, a computational framework allows for the integration of experimental and computational data using a variety of selected models. Therefore, a computational algorithm is useful to guide design optimization. A recent study indicated that efficiency for drug delivery can be improved by new agents/active compounds functionalized with nanoscale compounds[18]. In this context, the organic compound of methotrexate (MTX) is an anticancer drug commonly used to treat osteosarcomas. Primarily, it inhibits dihydrofolate reductase and inhibits tumor cell production, growth, and division[19,20]. However, problems occur with regular administration of chemotherapeutic agents, such as low efficacy, poor targeting, and significant toxic side effects[21-24]. The secret to increasing efficacy lies in how to effectively deliver the drug to tumor tissue[25,26]. Therefore, in recent years, various nanocarriers, such as functionalized groups of nanoparticles, such as liposomes, vesicles, and micelles, have been used to penetrate tumor tissue in large numbers and achieve a unique high permeability and retention (EPR) effect[27-52]. The EPR effect enables nanoparticles to passively penetrate tumor tissues by permeating the vascular endothelium of tumor tissues[32-34]. In this regard, nanotechnology has recently taken drug therapy to a new level and transformed medicine and drug delivery[42-50]. Nanodrug systems ranging in size from 1 to 100 nm in at least one dimension have been used as vehicles for drug delivery and offer several advantages, such as: For example, improved and prolonged targeting, reduced off-site targeting, reduced side effects and toxicity, improved drug solubility, improved pharmacokinetic parameters, overcoming drug resistance, continuous drug release, etc.[51,52]. Various carriers, including polymeric nanoparticles, lipid

nanocarrier liposomes, transferosomes, etc., and amphiphilic surfactant carriers, niosomes[53-57], are used for nanodrug delivery to achieve therapeutic goals. In this case, drug-loaded functionalized nanoparticles with water-soluble drugs were suboptimally anchored to the micelles by nanochemical processes. They are preserved by a hydrophilic micelle molecule fragment in the external environment, which increases the solubility of the drug in relation to water solubility. This type of drug-loaded nanoparticle depends on the external environment, which can precisely control the release of the drug[58]. To effectively address this problem, smart nanoparticles are currently being developed for measurement. Therefore, drug-loaded functionalized nanoparticles are crucial for the development of potential therapeutic sensors and medical imaging. On the other hand, the selection of functional groups/materials is another task, as each group behaves differently, resulting in different properties that affect different functions and applications. In this context, the use of functionalized polymer nanoparticles is a crucial strategy for improving drug bioavailability or precise distribution to the site of action. Polymers are unique materials that have characteristic properties and offer great synthetic versatility, allowing researchers to tailor them to specific needs or targets. However, when nanoparticles are used as drug carriers, the hydrophobic drugs can be grafted onto hydrophilic materials through chemical bonding to improve the solubility and bioavailability of the drug and increase the stability of the nanoparticles in the body.[59-63] Because of the importance of this relationship, poly-γ-glutamic acid (γ-PGA)-based micro/nanoparticles have attracted much attention in the last 10 years as antibacterial agents and for drug delivery because of their controlled and sustained release, low toxicity, and biocompatibility with tissues and cells. Due to their biodegradable, non-toxic, and non-immunogenic properties, they are also successfully used in wastewater, food, and medical industries. Research on chemotherapy and drug delivery systems is based on mechanisms of cell uptake. In addition, the conjugated scaffold of hydrophobic and hydrophilic models can penetrate the lipid membrane due to its dual properties. Although numerous studies have shown the pH-dependent effect of nanoparticle behavior on the mechanisms of cellular uptake through coarse-grained simulations,[64] cellular uptake mainly depends on size, shape and surface area,[65] and further variations in colloidal stability are also important factors in distinguishing the cellular uptake of nanoparticles in biological media rather than size, surface area and surface charge[66] (ζ). However, few studies[67] have been conducted that amount to full atomistic simulation studies that do not lack degrees

of freedom, charge, and structure. This is due to the complexity of the system one has to deal with in molecular modeling studies.

However, systematic knowledge of the factors affecting the physicochemical properties of drug-loaded nanoparticles and influencing the mechanism of cellular uptake at different pH values is very limited. To overcome this obstacle, the models I have designed to form MTX-SS-PGA from simulation studies (MD) are suitable for developing models that describe the cellular uptake of drug-loaded nanoparticles in a safe and sustainable manner and enable efficient drug delivery to cancer cells. Therefore, our computer simulation studies can support testing and aid in the logical development of novel formulations with increased efficacy. However, many other factors play a role in nanoparticle uptake, including the physicochemical properties of nanoparticles, protein–particle interactions, and subsequent agglomeration, diffusion, and sedimentation. The process of agglomeration mainly depends on the surface charge (zeta potential (ζ)) of the nanoparticle, which can stabilize the dispersed nanoparticle and prevent the process. Therefore, to control stability in a biological medium, many factors that affect the zeta potential (ζ) of the nanoparticles must be considered, including the complex interactions between the nanoparticles and the biological medium (PC). The dynamic and complex structure of this biological corona ensures that the host cell responds to the nanoparticles. To study the protein environment, many researchers distinguish between two protein layers: the "hard" and the "soft" corona[68,69]. The hard corona is responsible for the fate of biological nanoparticles, while the soft corona is usually responsible for irrelevant proteins that can easily be exchanged between the hard corona and the intermediate corona[70]. The composition of the protein corona changes with the surface area of the nanosystem. Therefore, changes in the intrinsic properties, such as size, charge, and surface geometry of the PNP, change the nature of the protein corona, which in turn affects the fate of the biological system. In this case, the proteins play a crucial role together with the coatings, which almost completely determine the stability and agglomeration of the nanomaterials. These two phenomena—stability and agglomeration—are essentially directly related to the cytotoxicity of the entire nanomaterial[71]. This is directly related to the degree of cellular absorptivity of the nanoparticle, which leads to the measurement of the risk assessment of the materials so that the development of new nanomaterials is always based on a comprehensive risk factor[72]. In general, a change in pH or ion concentration affects the surface charge and stability of nanoparticles in the medium[73], so it is extremely important to determine the zeta potential value of all

toxicologically evaluated nanoparticles. Numerous studies in the literature have attempted to experimentally characterize the zeta potential of NPs[74]. However, the relationship between the zeta potential, nanostructure properties, and toxicity of new untested NPs remains unclear. Therefore, computational methods have been developed to predict the quantitative relationship between the structure of NP[75(a)] and the zeta potential value. According to theoretical models[75(b),76] the zeta potential is influenced by the structure of intrinsic and extrinsic particle properties, such as size, concentration, and biological environment. However, in recent studies, little is known about how different surface modifications affect the quantitative and qualitative composition of the corona, how these modifications influence the zeta potential that controls stability, and how aggregation/agglomeration of functionalized NPs is limited in a given medium. To address this challenge, the integration of machine learning techniques based on the Genetic Algorithm – Partial Least Square (GA-PLS) and novel nanodescriptors that identify both intrinsic and extrinsic properties of NPs was used to significantly increase the potential of *in silico* methods to predict the zeta potential of NPs in a given biological medium and to achieve good correlation with experimental predictions[77]. Moreover, when these nanoparticles come into contact with biological fluids in the blood, a "corona" is formed on the surface of the nanoparticles, mainly proteins, as a result of the dynamic adsorption of biomolecules. The "corona" formed by the adsorbed NPs can drastically change the surface properties of the NPs and affect their biological behavior, leading to changes in the functionality of the NPs and the stability of the dispersion. Sometimes, these changes result in a loss or increase in NP functionality, which can also affect its toxicity, for example, biological distribution, uptake, opsonization, and kinetics[75(a)(b)] of NP. When an organism or cell ingests aggregated/agglomerated NPs, the NPs may break down into smaller particles depending on the environment, such as pH, concentration, and protein corona. The surface area may increase as the size of the NPs shrinks. As a result, scattered NPs can act like a "Trojan horse" (more like toxic ions) that becomes increasingly dangerous to humans and the environment[76]. To help this process be efficient, the design of chemicals that should be safe and sustainable is another challenge in detecting toxic ions at an early stage. To address this similar kind of issue efficiently, our computational framework plays a crucial role in the design of the appropriate chemical. Moreover, the detection of toxic ions (CN^- anions) in various samples, including water samples, is another difficult task, which is to develop a suitable functionalized organic functionalized material that has unique properties for the detection of CN^-, F^-, and so on. Since

anions, such as cyanide (CN^-), are among the most dangerous ions known to mankind and act as Trojan horses in the natural environment, it is also critical to detect them at very low concentrations[78]. In recent years, the search for hazardous cyanides in food and water has become an important challenge for the early compensation of this process in the natural environment. To protect human health, it is critical to develop rapid and effective methods for the detection of cyanides in real-time and in the environment. To meet this challenge, malononitrile-functionalized compounds have been widely used in recent decades for the detection of CN^- ions and many industrial applications, e.g., in the chemical, medical, and agricultural industries, due to the versatile and unique reactivity of the weak cyanocarboxylic acid of malononitrile. Gholamzadeh et al.[79] published a simple sensor, S29 (1,4-2,2-dicyanovinylbenzene), functionalized with malononitrile for the selective detection of CN^- ions versus various anions in DMSO/EtOH. The detection mechanism shows that CN^- can be detected by a nucleophilic attack on the carbon atom of the C=C group of S29, as shown by spectroscopic studies. For the detection of various ions, a simple 2-(4-(bis-(4-(5-methyl-2,4-dioxo-3,4-dihydropyrimidin-1(2H)-yl) oxy) phenyl)amino)benzylidene-malononitrile (BCTT) sensor (S31)[80] was described for the very sensitive and selective detection of Hg^{2+} and CN^- ions. Moreover, the color of the solution changed from colorless to yellow when CN^- ions were added to the sensor because they served as a base that abstracted hydrogen from the phenolic component of the molecule to produce the corresponding dye. A.D.S. Schramm et al.[81] proposed a chemosensor for the dye 2-(4-hydroxybenzylidene) malononitrile in which 2-[4(dimethylamino)benzylidene] malononitrile served as a ratiometric fluorescent chemosensor for CN^- ions in the sensor. The yellow dye solution turns from yellow to colorless in the presence of CN^- ions. This is because CN^- attacks the double bond CH=C in the molecule and breaks the electronic conjugation between the electron-donating and electron-accepting parts of the dye. Li et al.[82] designed and synthesized for 2-((2-phenyl-2H-1,2,3-triazol-4-yl)methylene)malononitrile to develop a new highly selective fluorescent chemosensor for the detection of CN^- ions compared to other anions in DMSO. During the development of the probe, colorimetric detection[83] gained popularity due to its high sensitivity and rapid detection by the naked eye compared to conventional methods. However, there is a great demand for colorimetrically detected organic sensing molecule probes[84] to detect CN^- ions, even at low concentrations in samples. To meet this demand, a suitable model of an organic functionalized material could have chemical properties for the detection of hazardous anions in samples,

which could have potential applications in human life. Furthermore, the conjugated functionalized material has sensing capability due to the mechanical effect of charge transfer from donor–acceptor units, and requirements have been developed to utilize the properties of an organic molecule as needed for a sensor[85-89]. In this context, the malononitrile-functionalized model developed for the rapid colorimetric detection of cyanide ion (CN^-) in the presence of a malononitrile-functionalized DMN probe ((2-[[7-[5-[bis(4-methylphenyl) amino]-2-thienyl]-2,1,3-benzothiadiazol-4-yl] methylene] propanenitrile) is based on blocking the intramolecular charge transfer mechanism in various samples, including water. In this communication, the ICT-based functionalized probe (sensor) of DMN exhibits a kind of donor-acceptor-acceptor (D-A'-A) characteristic, in which the conjugated parts of the ditolyl-aminothienyl group act as the electron-donating group, and the electron-withdrawing dicyanovinylene is bridged by the 2,1,3-benzothiadiazole part (BT) of another electron-withdrawing block with structural analogs. The stronger electron-donating group of the ditolylaminothienyl moiety confers a small band-energy gap[90] to the functionalized DMN probe due to the enhanced quinoid character and ubiquitous acceptor character of the BT moiety, which is used in optoelectronic materials due to the intriguing properties of the low-lying band gap, high absorption coefficient, and desired energy levels. This photophysical property allows the functionalized probe, commonly used in industry to detect cyanide-containing wastewater, to potentially detect ions. In this case, the malononitrile-functionalized DMN probe acts as a fast colorimetric detection with properties that allow the detection of cyanide in real samples, even at a lower concentration. Our specified computational framework will be useful for designing the functionalized probe at an early stage to detect toxic ions in various environmental samples, as described.

In the past, the development of new materials was based on experimentation and intuition. However, due to the high cost, long research time, and manual labor associated with experimental studies, there have always been significant obstacles to this method. There are many combinations of organic molecules, and the structural features of nanoparticles present significant difficulties in the development of functional materials, so it is not unreasonable to study them all experimentally to find the most efficient, safe, and sustainable functional materials with the desired properties. However, advances in theory, computer power, and numerical algorithms in recent years have enabled new simulation-based approaches to materials analysis that can be quickly and inexpensively applied to millions of materials.

Today, researchers are often able to analyze hundreds or even millions of materials on supercomputers in 'high-throughput' mode[91], which allows them to evaluate density functional theory calculations (DFT) that resolve the electronic structure of a material with few modifiable parameters. Several examples of new functional materials have been discovered using these computational methods and subsequently verified experimentally.[92] In addition, there is a difficulty that can be solved by applying appropriate computational frameworks that could prove useful in developing new functional materials with specific properties and finding new applications. In this context, the integration of different computer models of our specific computational framework for each case study is useful for the development and improvement of the properties of functional materials, which is why they are so important.

1.2. From Atomistic Approaches to Nano-QSPR Modeling: A Computational Framework

A computational framework allows for the fusion of experimental and computer-assisted data, a set of user-defined models, and a computer algorithm to control design optimization. However, the methods for modeling systems on different scales vary depending on the application. The literature data indicate that atomistic modeling and integrated models of nano-QSPR with machine learning may support the design process of safe and sustainable materials design before synthesis (at the virtual stage).

1.2.1. Atomistic approaches

Electronic Structure Modeling

The development of numerous physical models to derive the fundamental interactions of atoms and molecules was made possible in the 20th century by quantum mechanics. Spectroscopy, bonding, electronic motion, and nuclear motion all have properties that can be explained by these basic laws. Direct applications of large molecular or material systems are hampered by the complexity of physics caused by multi-body interactions. Approaches based on the Density Functional Theory (DFT) have been very popular in the industry because of their low computational costs, easy adaptation and considerable accuracy in predicting properties. These techniques have disadvantages in the calculation of excited states, which have been overcome by the time-dependent DFT methodology (TD-DFT)[93]. The exchange-correlation functionalities chosen to define the system have an impact on the accuracy of DFT

applications. In this context, the QM method is based on quantum-mechanical methods to show the chemical system. To solve the Schrodinger equation, numerous approximation values were calculated using this technique. QM Based on the above tools, which are very useful for our project with different functionalized materials, the Schiff-based functionalized pyrene derivatives of PS1 and PS2 were optimized with the B3LYP/6-31G* level theory to be possible in an energy-minimized structure without imaginary frequency. In addition, a HOMO-LUMO orbital analysis of the delocalized orbital orientation of the PS1 and PS2 compounds was performed to calculate numerous properties, such as energy gap, hardness, softness, electronegativity, electrophilicity index, chemical potential, and cytotoxicity. In the case of the malononitrile-functionalized DMN probe with and without CN^- ions, I have used TD-DFT theory to calculate the absorption spectra in the presence of the solvent tetrahydrofuran; our results are well in line with experimental methods. In particular, the properties of many different chemicals, biological systems, and physical systems have been successfully calculated using TD-DFT theory. In spectroscopy, where TD-DFT generates reaction characteristics and excitation of atoms, molecules, and solids, this technique is most frequently used to optimize the geometries of molecules, such as DMN or DMN-CN^- probes. During optimization, I used many different theoretical layers to predict how strong the influence of structure-property is, e.g., B3LYP, BP86, CAM-B3LYP, M06-2X, B3P86, and PBE functionals. Computer models are used in all research areas to evaluate property calculations and their impact on the environment. From the perspective of nanoscale materials, I used QM methods to calculate the descriptors for the core (polymer) and coating (functional) groups, and the properties were determined using the nano-QSPR method. The geometry of the MTX-loaded functionalized nanoparticles was then optimized using the B3LYP/6-31G* theory to obtain an energy-minimized structure that could generate force field parameters and start classical MD simulations.

1.2.2. Molecular Modeling: Docking and Molecular Dynamics

Although quantum-mechanics-based simulations, such as DFT, are very well suited to characterizing molecular systems, they are limited to a few hundred atoms due to the complexity of electronic interactions[94]. The main objective of molecular docking research is to mathematically simulate the molecular recognition process in order to understand it. Accordingly, molecular mechanics research must find an ideal conformation for the protein

and ligand, as well as their relative orientation, to reduce the free energy of the entire system. Systems with longer lengths and longer time scales must be simulated to understand the dynamics of complicated processes. From the outset, I dispense with methods of approximation, such as empirical parameterization of force-field models, which are models of atomic-atomic interactions, and follow the method of classical mechanics used to calculate the model system using Newtonian mechanics. It is possible to simulate systems with length scales of the order of ~10-1000 nm and time scales of up to ~100 ns using methods such as classical molecular dynamics (MD) and Monte Carlo (MC). These techniques use DFT calculations or experimental data to derive the parameters of the force field model. These computer techniques are often used to determine the properties of materials and transport of materials in environments where experimentation is difficult. Based on this application, I performed in-depth analyzes with computer techniques and supplemented them with experimental studies. The MD study illustrates the dynamic behaviour of proteins as a result of binding to ligands/drugs at different time intervals[95]. Molecular mechanics and the continuum solvent technique of MMPBSA are combined to further evaluate the binding energies of protein ligands/drug complexes[96]. Consequently, the results of these MD simulations are crucial for improving drug discovery and development methods. In this context, docking studies were conducted to investigate how well PS1 and PS2 bind to the BSA proteins. MD was used to analyze the interaction between the BSA protein and two different compounds, PS1 and PS2, using a computer simulation method to study protein–ligand interactions that take into account the stability and energetics of the system at all times. I then attempted to generate the PMF curve using two separate drug-functionalized nanoparticle models, MTX-SS-PGA and fully atomistic MD simulations at different organ sites, to determine the free energy barrier using MD-based umbrella samples and WHAM analysis approaches.

1.2.3. Machine Learning-Based Nano-QSPR Method

QSPR models are molecular-based prediction techniques that allow the prediction of quantifiable macroscopic properties "P" of compounds based solely on the molecular structure of this information and can therefore be used before compounds are synthesized. Following the principle of similarity, these models are based on the assumption that compounds with similar molecular structures have comparable properties. Links between the target property and several molecular structure descriptors were searched from a collection of molecules comparable to

those in the final model. The generic form in the equation provides a summary of the QSPR models (Eq. 1).

$$P = f(d_i) \quad (1)$$

The molecular structures of chemical compounds and their properties at the molecular level are described by molecular descriptors. Over time, thousands of descriptors (d_i) have been created to encode a wide range of compounds and their molecular properties. There are several types of descriptors, usually determined by quantum chemical calculations. They can be obtained from simple elementary formulas and 2- or 3-dimensional structures. I then used the most efficient genetic algorithm (GA) based on machine learning, which optimizes the descriptors based on the R^2 value to select the best result in the selection to select the most relevant molecular descriptors for the PLS method. GA was proposed by John Holland[97] to find a more comprehensive explanation and is a random search method to achieve optimized results. Based on these tools, I made the first attempt at a machine-learning model that quantifies the relationship between the structure and properties of NPs defined by the so-called core and coating descriptors, their PC fingerprints in the biological medium defined by the so-called corona descriptors, and their influences on the zeta potential value of the nano-QSPR model. The genetic algorithm and partial least squares (GA-PLS) were used to build the nano-QSPR model.

However, despite the numerous possibilities and advances made in the field of computer modeling to compensate for experiments, there are still problems that need to be solved. Unlike industrial aspects, where complex structures and compositions are commonly used, modeling usually uses pure/pristine materials, which leads to problems with accuracy. In this situation, the three most important challenges—predictability, realistic complexity, and material information systems—must be improved to take into account large-scale features and solve these problems. Wave function theories have been the basis for much quantum chemistry but improving them can be expensive and time-consuming. The opposite perspective of relying on approximate energy functions, which are mathematically cheap but have qualitative deficiencies, has proven very advantageous for material simulations. These qualitative deficiencies are particularly evident in some of the most useful functional materials, such as mixed valence transition metal oxides. In the future, more advanced functional theories will be developed that can address some of the fundamental qualitative deficiencies of current

approximations. In addition, there will be a stronger interaction between spectral theories that focus on the precise description of excitations and basic state formulations. Most of the developments in the field of material simulation over the past 30 years have been in the realm of realistic complexity and are not limited to static calculations. The effects of pressure, pH, chemical potentials, and electrochemical potentials, to name just a few, can now be added to the effects of temperature on the environment. From infrared and Raman spectra to nuclear magnetic resonance, electronic paramagnetic resonance, or angular-resolved photoemission spectroscopy, we can predict spectroscopic and microscopic data. By providing input to mesoscopic or macroscopic theories that relate directly to coarser formulations or by providing large training datasets of microscopic data for machine learning of atomic interactions, first-principle calculations can exceed length scales. Time constraints in the modeling of rare events can be solved by effective approaches that accelerate configuration sampling from metadynamics to replica exchange. Last but not least, the ability to automatically perform tens to hundreds of thousands of calculations gives us a comprehensive overview of the material landscape so that we can use systematic database-based, database-filling protocols to explore unexplored areas of material space, apply data analysis to find new insights or correlations, and formulate systematic collaborative efforts to curate and verify material properties. Furthermore, there are no automated models to study variations in the composition or structure of complex systems, and there is no consistent method to predict the properties of coated functionalized materials. Although many computational challenges need to be compared with reality, they will be very useful for characterizing and designing functional materials with suitable properties and obtaining useful applications. Therefore, new approaches, such as machine learning, big data, and soft computing, are needed as tools to compensate for the limitations of classical experiments, which entail high costs, short test times, and other difficult conditions. In addition to experimental characterization techniques, which only provide the average/integral properties, computer models can capture the missing properties of nano/microstructures in complex materials. Therefore, computer methods will function as a creative center between science and technology by evaluating, understanding, and ultimately converting these phenomena into materials.

2. Statement of Research Problems

Organic compounds play an important role in human functioning, including carbohydrates, proteins, lipids, and nucleotides. In this context, organic compounds functionalized with Schiff bases are widely used for dyes, pigments, catalysts, luminescence, chemosensors[98], polymer stabilizers[99], and organic synthesis intermediates[100]. SBs are also used as corrosion inhibitors in various metal electrolyte systems, as biolubricant additives in tribology[101-104], as CO_2 fixation catalysts for environmental protection[105], in carbohydrate research[106], in photoactive solar energy[107,108] and as vitrimers[109]. Currently, SBs contribute more to biological chemistry than pharmaceutical applications with antibacterial properties. However, many of the drugs on the market for bacterial infections rarely reach the efficiency factor, as multidrug-resistant bacteria (MDRBs) are likely to cause the failure of treatment. One of the most promising compounds is related to SB-functionalized pyrene derivatives. The number of research publications on pyrene and its derivatives is increasing. For example, in recent studies by Srinivasan et al.[15], functionalized Schiff-based pyrene compounds were synthesized. The developed pyrene compounds were tested for their antibacterial activity against various bacterial strains. However, to date, knowledge of the binding mechanism with proteins, such as BSA, is very limited. To overcome this problem, I applied a framework of numerous computational programs, such as QM, DOCKING, MD, and MMPBSA, to design new SB-functionalized pyrene derivatives that showed improved antibacterial activity compared to previous compounds. The application of computational methods may provide information on the conformational state of the binding of the drug (compound), the binding affinity of the drug, and the native-state of the chemical reactivity of pyrene compounds, which may help improve the antibacterial activity of newly synthesized SB-functionalized pyrene derivative compounds when they interact with protein albumin. The efficacy of drugs (organic compounds) can be improved if they are loaded with nanoscale compounds. Recent studies on nanomedicine[110] play an important role in the field of drug delivery, as nanomedicine can deliver the drug efficiently and without greater side effects than conventional delivery methods.

However, in nanomedicine, it is difficult to determine the mechanisms of cellular drug uptake and delivery. The problem could be overcome by the application of proper theoretical models that determine the mechanism in three different organs of the human body to understand the cell uptake mechanism. The determination of how the structure, charge, and energy of NP affect the different pH values (e.g., from the neutral pH to the medium pH in the

tumor, and the pH in the stomach) could help to understand the relationship between the cell-uptake mechanism and nanoparticle structure. The data available in the literature suggest that coarse-grained MD simulations could support this process. For example, Zhang et al.[111] have demonstrated that cellular uptake depends mainly on the parameters of size, shape, and elasticity of NPs, but the full atomistic approach to the interaction of drug-loaded nanoparticles with the cell membrane is very limited. Lei Zhang et al.[112] have shown the effective role of anticancer drugs in the presence of cholesterol lipid bilayer uptake mechanisms. However, until now, no studies and molecular models have applied full-atomistic MD simulations to predict the mechanism of cellular uptake, starting from neutral pH to pH in the tumor and pH in the stomach. However, we should keep in mind that the mechanism of cell uptake may be influenced by many other factors, not only the physicochemical properties of nanoparticles, but also protein–particle interactions and subsequent agglomeration, diffusion, and sedimentation. The agglomeration process depends mainly on the zeta potential (ζ) (surface charge) of the system. In recent decades, the important factor for predicting the zeta potential (ζ) of unmodified NPs has played a crucial role in determining the stability, toxicity, and aggregation/agglomeration process of NPs[75(a)]. In this context, previous work by Mikolajczyk et al.[75(a)] used the quantitative nanostructure-property-relationship (nano-QSPR) method and nanostructural descriptors to estimate the zeta potential of various metal oxide nanoparticles. To predict the zeta potential of various metal oxide nanoparticles affected by the action of an ionic solution (KCl), Wyrzykowska et al.[75(b)] used a developed nano-QSPR technology. The authors[113] also presented a structure-property relationship model (nano-SAR) to predict the zeta potential values of nanoparticles evaluated in different environments, such as pH, the presence of ions (Na^+, K^+), and under different culture conditions. However, little is known about how different surface modifications affect the quantitative and qualitative composition of the corona and how they affect the zeta potential that controls the stability and aggregation/agglomeration of functionalized NPs in a given medium. Furthermore, no information is known about how a particular corona composition affects the uptake of NP and its associated toxicological profile.

Therefore, one of the most difficult and important problems for computational toxicologists is developing new methods for conventional computational models that can link the zeta potential (ζ) and the core, coating, and corona of NP. To overcome this obstacle, we hypothesized that combining machine learning techniques based on the partial least squares

(GA-PLS) genetic algorithm with novel nanodescriptors that identify both the intrinsic and extrinsic properties of NPs would greatly improve the ability of *in silico* methods to predict the zeta potential of NPs in a given biological medium. Through these applications, I learned how the surrounding protein corona affects the zeta potential in terms of the quantitative relative relationship between the coated NP structure and the biological medium. The main goal of the project was to demonstrate the importance of considering how PC can affect the physicochemical properties of functionalized (coated) polymeric nanoparticles. For the development of safe and sustainable materials, our modeling method could be very useful because as NP enter the cell, adsorption leads to the formation of an agglomeration of NPs. The scattered NPs are like Trojan horses for toxic ions due to the surface area-to-volume ratio, which is even more harmful to humans. To assist this similar kind of process, there is a space for designing functional materials that are urgently needed and treating similar types of problems for humanity. In this context, toxic ions, such as CN^-, are found in food and water samples. To solve this problem, organic functionalized probe molecules have been widely used in recent decades to capture toxic ions in various samples[114]. However, the rapid detection of CN^- ions at lower concentrations using selective detection colorimetric methods is very limited. Therefore, an ICT-based malononitrile-functionalized DMN probe was modeled for easy and rapid detection of CN^- ions in samples using a naked-eye colorimetric probe supported by experimentalists. Recently, the detection of CN^- ions in the probe has been proposed in solutions covering major practical applications, such as agricultural products, cassava powder, bitter almonds, smartphones, test strips, and sensors. Based on these facts, I worked on a project for the rapid detection of CN^- ions in a malononitrile-functionalized DMN probe with and without housing using a colorimetric method. To model the probe and find the mechanism of the interaction of the DMN probe with CN^- ions via an intermolecular interaction process, I calculated absorption spectra using QM/TD-DFT calculations that correlated well with experimental data, along with HOMO-LUMO orbital analysis and found the behavior of the probe with and without CN^- ions. In addition, an open-source application for Android and a portable 3D-printed smartphone accessory was developed to work with the DMN probe in the field. Finally, the migration of organic functional materials to nanofunctional materials will be useful for various potential applications because of the unique physicochemical properties and the different environmental systems that affect the various functional properties. Based on the fact that applications are possible, our goal was to investigate the behavior of organic and

nanofunctionalized materials under different environmental conditions and to design safe and sustainable materials for many different applications.

The objectives of the research conducted in my dissertation were:

(i) The development of a computational framework based on various computational tools such as QM, DOCKING, MD, and MD- supported by MMPBSA to design new functional materials PS1 and PS2 with the properties of improved free energy binding and low energy gap, which can be used as a material with improved antibacterial properties, and

(ii) The application of computational models based on MD and MD, which are based on the umbrella sampling methods, to gain systematic knowledge about the influence of drug-loaded functional nanoparticles on cell uptake at different pH values to develop an efficient drug delivery medium.

(iii) The development of a new type of descriptor for describing the core, coating, and corona of functionalized NPs, together with the development of a nano-QSPR model describing the relationship between the physicochemical properties and the zeta potential value of functionalized NPs in a biological medium, which may be crucial to enhance the stability of functionalized NP-based drug delivery.

(iv) The application of the theoretical framework based on the QM/TD-DFT method to control the functionalized probe of DMN with the features of rapid colorimetric detection of CN^- ions with the possible elimination of toxic ions in humans in the environment.

3. Main Hypotheses

Hypothesis 1

I hypothesize that the interaction of bovine serum albumin with the newly synthesized Schiff-based functionalized pyrene derivatives PS1 and PS2 will have a superior antibacterial character compared to similar previous studies. I hypothesize that a framework of computer tools can be used to design a better antibacterial character of Schiff-base functionalized pyrene derivative compounds by predicting the binding affinity, chemical reactivity, and cytotoxic activity of the compounds, as well as the potential efficacy of all compounds, on the basis of experimental evidence.

Hypothesis 2

The cell membrane itself is a major barrier that drug molecules cannot easily penetrate, which is why many drugs fail in the clinical trial phase. Overcoming this challenge is a major burden for science. MTX (methotrexate), an anticancer drug-enhanced grafted with γ-polyglutamic acid (PGA), acts as a hydrophilic nanocarrier that is passively taken up by cells at neutral pH, as experimental observations have shown, with lower concentrations and toxicity. Cellular uptake mainly depends on pH and structure, charge, and energy properties, and the insights found from MD suggest important factors for understanding drug delivery. I hypothesize that the computational models of MD studies can predict the cell uptake mechanism of drug-loaded polymer-functionalized nanoparticles for neutral, tumor, and stomach pH models. MD studies for various analogies may help to understand how the charge, geometry, and energetics of drug-loaded functionalized nanoparticles affect cellular uptake at three different pH levels: neutral pH, tumor pH, and stomach pH of 7.0, 6.4, and 2.0, respectively.

Hypothesis 3

Characterization of the zeta potential (ζ) is one of the most important challenges in understanding how the stability of NP and the formation of the protein corona affect the biological reactions of cells and organisms. In this context, we hypothesized that the integration

of machine learning methods based on the genetic algorithm of partial least squares (GA-PLS) and novel nanodescriptors that determine both the intrinsic and extrinsic properties of NPs would significantly increase the potential of *in silico* methods for predicting the zeta potential of functionalized (coating) NPs in a given biological medium. Furthermore, a predictive nano-QSPR model may help describe the relationship between the structure of polymer NPs, represented by the core, coating, and corona properties, and the zeta potential in a biological medium.

Hypothesis 4

I hypothesize that the presence of cyanide ions in the functionalized DMN probe blocks intramolecular charge transfer between the dicyanovinyl group and the ditolylaminothienyl group, since a Michael adduct of the β-conjugated position of the dicyanovinyl group with cyanide forms. I hypothesize that a computer-aided and spectroscopic method may support the rapid colorimetric detection of hazardous ions from the sample and may be applied to the intermolecular interaction of an intramolecular charge-based malononitrile-functionalized DMN probe with cyanide ions (CN^-) from many samples or water samples in the naked-eye scenario.

4. Case Studies

4.1. Case Study 1

The first part of my dissertation is presented in the paper "Integrated Approach to Interaction Studies of Pyrene Derivatives with Bovine Serum Albumin: Insights from Theory and Experiment" (**attached as publication [A]**). In this article, I propose investigating the relationship between bovine serum albumin and recently synthesized very potent Schiff-based functionalized pyrene derivatives PS1 and PS2, which may have the advantage of having a superior antibacterial character, as reported in a previous report on related compounds[115]. The interaction and dynamic behaviour and conformational orientation of the two compounds in the BSA complex, PS1 and PS2, were predicted under physiological conditions of pH = 7.1 using molecular docking and molecular dynamics simulations. Furthermore, the molecular surface mechanics (MMPBSA) of Poisson-Boltzmann was used with Gromacs software to determine the free binding energies of the BSA-PS1 and BSA-PS2 complexes at 300 K. Our expected results and the experimental data showed a good correlation. Therefore, our modeled methodology can confirm the usefulness of our developed compounds for future research.

Methodology

The initial structures of the compounds PS1 and PS2 were created using Avogadro 1.1.1[116] and then geometrically optimized using the Gaussian 09 package[117] using DFT theory with the exchange-correlation of the functional functions B3LYP with the base set 6-31+G*. Energy-minimized optimized structures confirm the absence of imaginary frequencies using vibration frequency techniques. The Kohn–Shan diagram is a useful derivative of functional density theory to find a solution for several functions of the one-electron wave that depend only on three spatial variables and are non-interacting systems. The Hamiltonian of the single-electron system is as follows.

$$[-\hbar/2m_e \nabla^2 + V(r) + V_H(r) + V_{XC}(r)] = \phi_i(r) = \epsilon_i(r)\,\phi_i \quad (2)$$

Here, the sum of the three potentials V, V_H, and V_{XC} is shown on the left side, and the total energy is shown on the right side ($\epsilon_i(r)\,\phi_i$). The first potential describes how an electron interacts with a group of atomic nuclei. The second potential is known as the Hartree potential, which defines the Coulomb repulsion between the electrons that are being taken into account in one of the Kohn-Sham equations and the overall electron density that is determined by all

the problem's electrons. The third potential is known as the exchange-correlation potential (XC), and it incorporates all interactions, including all the implications of quantum mechanics that are not taken into account in the other potentials.

To obtain the molecular dynamics simulations of the BSA–PS complex, the first confirmation was extracted from the docking studies. In this context, the geometrically optimized structures of the PS compounds were docked to the BSA protein. A combined protocol with the binding mechanism for flexible drugs and rigid protein structures was performed using Auto Dock 4.0. Since the torsion bonds moved freely and the BSA was in the rigid mode, docking calculations were performed with Lamarck's genetic algorithm (LGA)[118]. Fifty independent runs with a population size of 150 and a maximum energy point of 25,000 Before the docking calculation, Auto Grid 4.0 developed energy network maps for each type of ligand atom.

To describe the docking studies, the force field contains an explanation of the free energy scoring function with six pair-wise scores (V) and an estimate of the conformation entropy lost when binding (S_{conf}).

$$\Delta G = (V^{L\text{-}L}{}_{bound} - V^{L\text{-}L}{}_{unbound}) + (V^{P\text{-}P}{}_{bound} - V^{P\text{-}P}{}_{unbound}) + (V^{P\text{-}L}{}_{bound} - V^{P\text{-}L}{}_{unbound} + \Delta S_{conf}) \quad (3)$$

Here, L and P are in a ligand-protein docking calculation for "ligand" and "protein," respectively.

The values for dispersion/repulsion, hydrogen bonding, electrostatic, and desolvation are all contained in pair-wise energetic terms:

$$V = W_{vdw} \sum_{i,j} \left(\frac{A_{ij}}{r_{ij}^{12}} - \frac{B_{ij}}{r_{ij}^{6}}\right) + W_{hbond} \sum_{i,j} E(t) \left(\frac{C_{ij}}{r_{ij}^{12}} - \frac{D_{ij}}{r_{ij}^{6}}\right) + W_{elec} \sum_{i,j} \frac{q_i q_j}{e(r_{ij}) r_{ij}} + W_{sol} \sum_{i,j} (S_i V_j + S_j V_i) e^{-\frac{r_{ij}^2}{2\sigma^2}} \quad (4)$$

The first term has a standard dispersion/repulsion potential of 6/12. The second term is a directed H-bond term with a potential of 10/12. The third term is the Coulomb potential for electrostatics. The last term is the desolvation potential, which is weighted by a solution parameter (S) and an exponential term with a distance rating factor of 3.5.

For the classical MD simulations, conformists of the complex form of the BSA-PS compounds from the docking studies were used. For all MD simulations and trajectory analysis, the Gromacs 2020.2[119] software package was used, which combines the AMBER99SB force field with the TIP3P water model.[120] To reduce the energy of the conjugated gradient, the BSA-PS complex was initially energetically reduced with 3000 steps of the steepest descent method and then with 2000 steps. For the system without position restriction, the equilibrium runs after 1 ns to enable stabilization of the system. The water molecule was investigated with RMSD (root mean square deviation), the dielectric permittivity of ε =1 in the 2-fs time step, the Maxwellian distribution for the initial velocity at the initial temperature, the Ewald algorithm for the particle network, the LINCS[121] algorithm for the limitation of all heavy atoms except hydrogen, the SETTLE[122] algorithm for the water molecule, and the Maxwellian algorithm for the electrostatic term. VMD and Gromacs were used to perform the trajectory analysis.

The formation of the macromolecular AMBER force field is described in the following for classical MD simulations.

$$E=\underbrace{\sum K_b(r-r_o)^2}_{\text{Bonds}}+\underbrace{\sum K_\theta(\theta-\theta_o)^2}_{\text{angles}}+\underbrace{\sum K\varphi[1+\cos(n\varphi-\delta)]}_{\text{dihedrals}}+\underbrace{\sum K\psi(\psi-\psi_o)^2}_{\text{improper}}+$$
$$+\underbrace{\sum_{i>j}\varepsilon[(r_m/r)^{12}-2(r_m/r)^6]}_{\text{Vdw}}+\underbrace{\sum_{i>j}(q_iq_j/4\pi\varepsilon_o\varepsilon_r)}_{\text{Columbic term}} \quad (5)$$

The sum indices run in the first three terms over all bonds, angles, and dihedral angles of rotation, defined by the covalent structure of the system, but in the last two terms, over all pairs of atoms that are not chemically bound and are instead separated by the distances $r_{ij} = | r_i - r_j |$ or by the point charges q_i.

From a physical point of view, the first two terms describe the energy of the deformations of the bond length "r" and the bond angle "θ" about their respective equilibrium values "r_0" and "θ_0". The harmonious form of these variables, together with the force constants K_b and K_θ ensures the correct chemical structure, but modeling chemical changes, such as bond breaks, is not possible. 'K' defines the height of the rotation barriers, 'n' is the periodicity, and the third term refers to the rotations around the chemical bond. The electrostatic Coulomb potential

is the last term, and the fourth term describes the interatomic van der Waals repulsion and attraction forces in the sense of the Lennard–Jones-12-6 potential. The van der Waals parameters ε and r_m, together with correctly set partial charges of Q_i and an effective value of the constant k, can explain some behaviours resulting from a certain environment.

We then used the g_mmpbsa[123] tools from Gromacs to calculate the free binding energy using molecular mechanics/Poisson-Boltzmann surface[124]. Each snapshot was selected from all 200 ps in a total of 4000 configurations.

Based on formula (6), the binding free energies are calculated as follows:

$$\Delta G_{complex} = G_{complex} - (G^{BSA} + G^{compound}) \quad (6)$$

The binding free energies of the complex BSA and PS compounds are represented by:

$G_{complex}$, G_{BSA} and $G_{compound}$, respectively. Formulas 8 and 10 can be used to express each term:

$$G_{Total} = E_{MM} + G_{sol} - TS \quad (7)$$

E_{MM} stands for "molecular mechanics," G_{sol} stands for "soluble free energy," and TS stands for "conformational entropy on ligand binding". High computing costs and limited predictability[125] have led to this being ignored.

The parameters of the molecular mechanical force field (MM)[126] were used to calculate the energy values, and the potential energy for the vacuum, E_{MM}, is composed of the energy of the bond and the non-bonded interactions.

$$E_{MM} = E_{bonded} + E_{nonbonded} = E_{bonded} + (E_{vdW} + E_{elec}) \quad (8)$$

In this case, the energy conditions for bonding, angles, dihedral, and inappropriate interactions are contained in E_{bonded}. $E_{nonbonded}$ determines the conditions of Coulomb and Lennard-Jones's potential functions for obtaining electrostatic (E_{elec}) and van der Waals (E_{vdW}) interactions. The single-trajectory approach assumes that the bound and unbound conformations of the protein and the ligand are identical. Therefore, the E_{bonded} bond is always zero[127].

Equation (9) describes the molecular mechanism:

$$E_{MM} = G_{vdw} + G_{elec} \quad (9)$$

In this case, the polar and nonpolar conditions of the contribution conditions were used to determine the solvent energy, as indicated in Eq. 10.

$$G_{sol} = G_{elec,sol} + G_{nonpol,sol} \qquad (10)$$

Results and Discussion

According to our analogy, I have used many different tools to achieve many useful results, such as optimizing the structures using the QM method in the Gaussian package. Since the dihedral angle of the atoms was measured as 180° for PS1 and 90° for S33-C34-C37-C38 in PS2, the geometry-optimized structure of PS1 has planar geometry and PS2, a nonplanar geometry, as shown in Figure 2. A phenyl ring perpendicular to the pyrene ring replaces the terminal methyl group of the hydrogen atom in PS1 to PS2. The FMO representations of PS1 and PS2 show several organic molecules with known electronic transitions, including π→π*, n→π*, and π(donor)→π*(acceptor). Using this notation, I can see that the electronic transitions for both compounds obey the HOMO-LUMO and HOMO-1-LUMO+1 transitions and are represented by the π→π* and n→π* transitions to distribute the LUMO orbitals of n→π* throughout the π-ring, for the HOMO-1-LUMO+1 transitions, only the nonbonding orbitals (n) are located on the π-ring side of the molecule, while for the π→π* transitions; the charge moieties of PS1 are only on the π-ring of the HOMO. The same behavior was observed with PS2. According to the report,[128] in this case, there is also increased chemical reactivity, which is related to the fact that its HOMO-LUMO energy gap is smaller than that of the Schiff bases (2.43 eV), which highlights the properties of compounds being developed for a variety of applications. It can be argued that PS1 and PS2 have similar reaction-promoting media in chemical reactions.

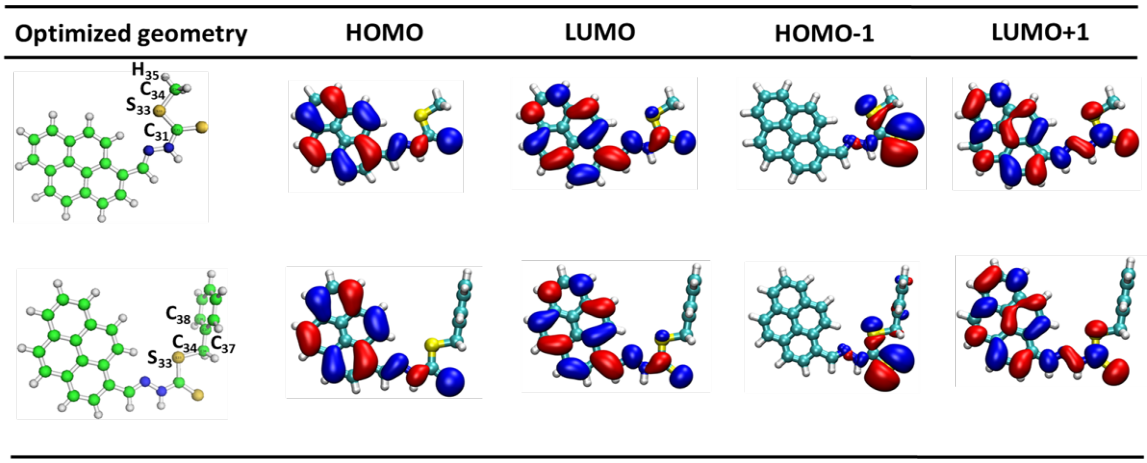

Figure 2. shows the compounds PS1 (top) and PS2 (bottom) with optimized geometry and HOMO/LUMO levels. Reprinted (modified) with permission from source[129]; Copyright 2022 American Chemical Society.

According to the QM calculations, I performed docking calculations to determine the possible orientation and binding of the free-energy values of the two compounds. According to the calculations, PS1 and PS2 have binding energies of -7.44 and -8.64 kcal/mol, respectively. Compared to PS1, the binding energy of PS2 is lower. The reason for the difference in the binding energy may be the presence of the dominant force of the interactive term vdW + hydrogen bond + desolve energy in PS2 compared to PS1 (-10.37 and -8.50 kcal/mol respectively). Although PS1 has two hydrogen bonds, resulting in a stronger binding affinity in the binding pocket, PS2 has a hydrophobic (benzene ring) than PS1. This leads to a greater hydrophobic interaction potential in PS2 compared to PS1, which leads to a higher binding affinity and lower free-energy binding values. Residues Arg256, Tyr149, and Arg198 form hydrogen bonds that bind BSA to PS1 and PS2. In addition to hydrogen bonds, hydrophobic and cation-π interactions are also possible in the BSA-PS1 complex, and π-π interactions are present in the BSA–PS2 complex (see Figure 3). Although many interactions were possible in both complexes, a stronger hydrophobic interaction was observed in the BSA–PS2 complex, which led to a higher binding affinity than in the BSA–PS1 complex, which was also confirmed in the experimental report.

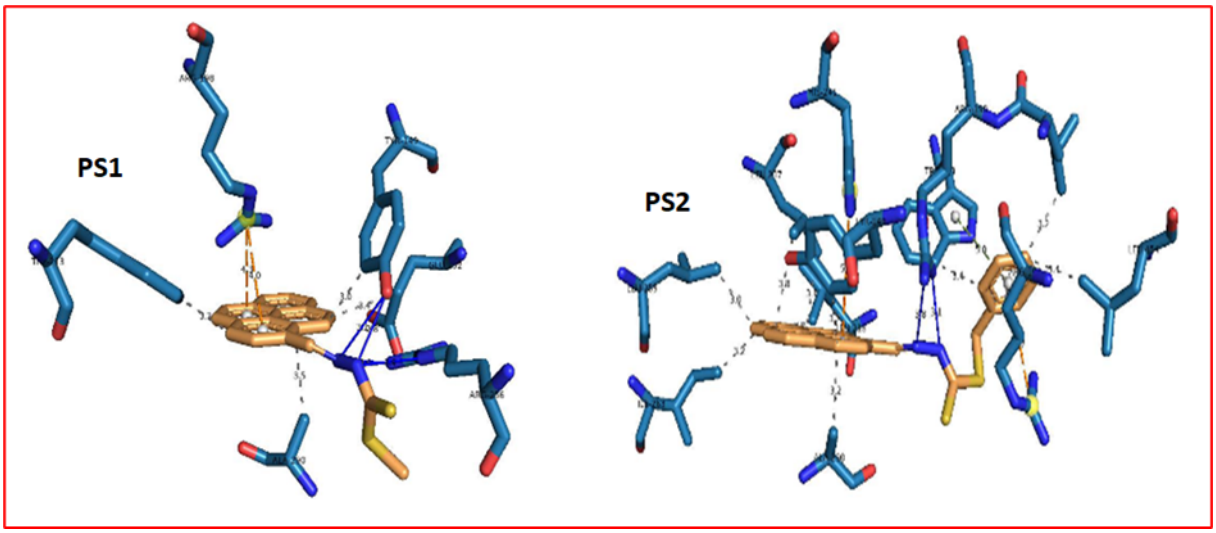

Figure 3. The docking sites for the two compounds, PS1 and PS2, are shown. Reprinted (modified) with permission from source[129]; Copyright 2022 American Chemical Society.

In the study of protein–ligand interactions using molecular dynamics (MD), a popular computer simulation technique, the stability and energetics of the system are taken into account at all times. In the present work with MD, the interaction between the BSA protein and two different compounds, such as PS1 and PS2, was investigated. For the two compounds, I performed a simulation with a duration of up to 40 ns at 300 K and considered the trajectories to determine the stability of the system and the binding site (see Figure 4).

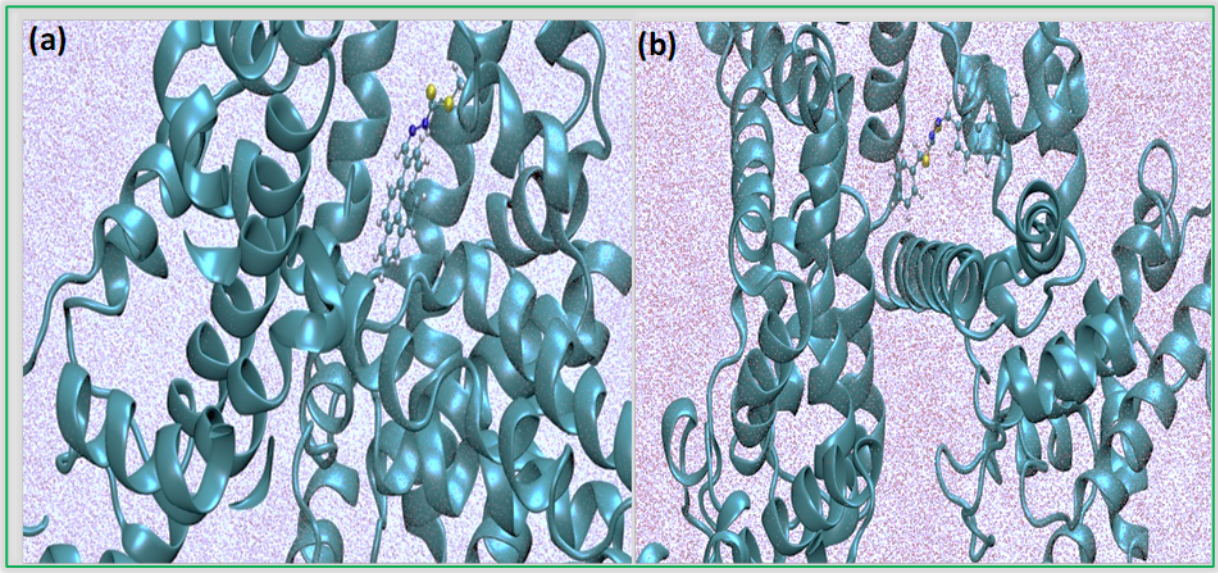

Figure 4. Conformational orientation of (a) PS1 and (b) PS2 in a complex with BSA. Reprinted (modified) with permission from source[129]; Copyright 2022 American Chemical Society.

Using MD simulation studies, I analyzed the binding mode behavior of both complexes at different time intervals, such as 15, 20, 30, and 40 ns, for both compounds. The results are based on the RMSD and RMSF analyses of the two complexes. The system approaches equilibrium at 1 ns for both complexes, which corresponds to the root mean square deviation (RMSD) between the Cα atoms of the coordinated complexes of PS1 and PS2 at 300 K compared to the reference structure of the original coordinates. Due to the stronger interactions between BSA and PS2 than PS1, the presence of more hydrocarbon (benzene) as a sterile factor in the PS2 compound, and the RMSD deviations of 3.0 for PS1 and 4.0 for PS2, the BSA-PS2 complex is comparatively more stable than the PS1 complex, and the RMSF analysis of the complex and fluctuating residues is equally effective up to a path profile of 40 ns for the BSA-PS1 and BSA-PS2 complex residues.

In this example, BSA-PS2 has the lowest free-binding energy of -138.50 kJ/mol, while BSA-PS1 has only -99.30 kJ/mol, indicating that the binding affinity of BSA-PS2 is greater than that of BSA-PS1; the values are shown in Table 1. Thus, the results show that MD and docking follow the same path.

Table 1. Binding free energies for BSA–PS complexes

Complex	Binding free energy (ΔG) in KJ/mol
BSA_PS1	-99.30 (1.6435)*
BSA_PS2	-138.50 (1.1804)*

*States the standard mean error. With permission from source[129]; Copyright 2022 American Chemical Society.

In summary, I investigated the binding affinity of PS1 and PS2 to intrinsically fluorescent plasma proteins using computer-assisted methods. To better understand the binding mechanism and the interaction of PS1 and PS2 with the BSA protein, molecular docking studies were conducted for these complexes, BSA-PS1 and BSA-PS2. The structural alignment of the two compounds within the BSA protein was investigated using molecular dynamics, and the binding energies of PS2 and PS1 calculated from computer simulations were -138.50 and -99.30 kJ/mol, respectively. Consequently, PS2 exhibited a higher affinity compared to PS1. Compared to BSA-PS1, the calculated free energy values of BSA-PS2 were more stable: the orbital orientation of the two compounds following the same orbitals π→π* and n→π* such as HOMO-LUMO and HOMO-1-LUMO+1 was investigated using FMO analysis, and finally, cytotoxicity studies were performed to determine the relative cytotoxicity of these compounds PS2 > PS1.

4.2. Case Study 2

The second part of my doctoral thesis is presented in the paper "How does the study MD of pH-dependent exposure of nanoparticles affect cellular uptake of anticancer drugs?", which is **attached as publication [B]**. In this project, I proposed how the charge, structural geometry, and energetics of drug-loaded NPs influence the cellular uptake mechanism with different pH levels and influence the drug delivery process. Based on the research question, I have used three different pH models, namely 7.0, 6.4, and 2.0, and the open-source program dimorphite-DL[130], to generate the molecular structure. The cellular uptake mechanism was proposed by analyzing the free energy barrier using classical MD- and MD-based umbrella sampling methods supported by the WHAM tool. Our primary research objective is to determine the extent to which different structural analogies, geometries, charges and energetics influence cellular uptake at different pH values. This is the first study with these models because, although many studies have been conducted on nanoparticles of size, shape, and surface and their influence[65] on the cellular uptake mechanism, I chose this problem because of the way the charge, structure, and energy of drug-charged nanoparticles affect cellular uptake by these parameters, as these studies have been very limited recently.

Methodology

All two models were created using the Dimorphite-DL[130] program. After the SMILE program has obtained a molecular geometry optimized with the B3LYP exchange-correlation function of the 6-31G* basic theorem using the DFT theory of the Gaussian 09 package[117], it provides formatted structural information with the corresponding pH values and then searches the pKa values from the database to generate, with the help of this optimized functionalized nanoparticle geometry, all possible conformations of the structural analogues in the form of a SMILE-formatted pH file. With energy-minimized conformations, vibration analysis without imaginary frequency was used to confirm the optimized geometries of the three pH models. Using the CHARMM GUI[131] membrane and the CHARMM36 FF[132] force field for lipids, three models of MD simulation were performed: 1. pH 7.0 of drug-loaded functionalized nanoparticles; 2. pH 6.4 and 3. pH 2.0 models consisting of a traditional POPC membrane with 64 lipids per leaflet. A TIP3P water model with additional CHARMM36 force-field parameters was used for all passes. The use of TIP3P[133] water molecules to solve the created model reduced

the total charge that replaced the counterions in the model. For each simulation box, the neutrality of POT^+ and Cl^- was added to the membrane composition. Each structural model was placed in the dissolved membrane simulation box and subjected to[133] different equilibrium processes using a multi-stage protocol. To keep the membrane stable and allow the water molecules to balance, seven different types of short-term equilibrium steps were performed using different thermostat conditions, force constants with different position limitation values, and others. For the periodic condition, the isothermal-isobar ensemble (NPT) was used, in which all h-bonds with atoms were subjected to the limitation technique LINCS[134]. During a spatial cut-off of 12 Å, the Ewald particle network method Ewald (PME)[135] was used for the extraction of all electrostatic interactions with a wide range. A cut-off value of 10 Å was used for the application of the Lennard–Jones interactions, which was then reduced to 12 Å. To detect all covalent bonds associated with hydrogen atoms, a holonomic restriction was implemented in conjunction with the SHAKE[136] algorithm. Gromacs 2020.2 software was used for MD simulations and analyzes[137].

Another possibility is to calculate the division of the three models between the membrane and the water in the vicinity. Above the aqueous phase of the water, the three models were positioned. In the semi-isotropic NPT ensemble, the drug-loaded nanoparticles were pulled toward the membrane centre with a tensile force of 1000 kJ/mol.nm^2 and a tensile velocity of -0.2 nm/s. A total of 30 windows were used to generate the PMF curve, taking snapshots at an interval of 1 Å from the upper (z = 30) to the centre (z = 0) of the simulation. The same is reflected in the remaining half of the track due to the symmetry of the double layer. The reflection measurements for the windows at 30 and 29 in the centre of the double layer are identical throughout the distance from this point on. Using a force constant of 1000 kJ/mol.nm^2 and a total sample of 1 μs nanoparticles entering the membrane, a production run of up to 1 ns was performed in each window. Configurations were recorded every 1 ps during the simulation, and at the end, biased, distributed, and reweighted analyses were combined with the WHAM[138] analysis to generate the PMF curve. Area analysis per lipid was used to obtain the molecular packaging of the lipid bilayer from the MD simulations. The APL value information provides information on the organization of lipids and the dynamic and structural properties of the membrane. The normal double layer is taken into account when calculating the APL along the z-axis. Equation 11 calculates the APL.

$$APL = \frac{L_x L_y}{N_{lipid}} \qquad (11)$$

The lengths of the box direction in x and y are represented here by L_x and L_y, the lipid content of a package by the number N_{lipid}.

The order parameter S_{CD} can identify the lipid acyl chains present in the lipid bilayer to determine how C-D is oriented relative to the typical bilayer. Equation 12 can be used for the calculation.

$$S_{CD} = 0.5 <3\cos^2\boldsymbol{\theta} - 1 > (12)$$

Here, < > determines an average ensemble, and "**θ**" indicates the angle between the normal double layer and the vector that connects C-D (C-H in our simulation example).

The diffusion coefficient resulting from Equation 13 is used to characterize and measure lateral diffusion, which is a crucial dynamic attribute for measuring the ability of lipids to flow through leaflets.

$$D(\tau) = \lim_{\tau\to\infty} (MSD(\tau)/4\tau) \qquad (13)$$

where "t" is the elapsed time and MSD is the average of the number of lipids and the mean square displacement (MSD) of the selected lipids in the mass centre of the XY plane.

Results and Discussion

The cellular uptake mechanism was determined by geometrically optimized MTX-loaded functionalized nanocarrier molecules with three alternative models of structural analogies. The geometry of the three models is almost cage-like, corresponding to their structural equivalents, as size[65] is a critical factor in cellular uptake. Our models are cage-shaped, spherically symmetric nanoparticles that are more easily absorbed because, according to this report,[139] spherical nanoparticles are more clearly and better uptake by cells than rod-shaped particles. According to these data,[140] the pterin portion of the methotrexate drug is crucially important for antimetabolite activity because it has a high affinity for the cellular enzyme dihydrofolate reductase, which changes when the activity of the drug is reduced. Because the hydrophobic core of the pterin moiety easily penetrates the hydrophobic tail of the lipid membrane and thus

influences drug activity, we hypothesize that the variation in the dihedral angle affects cell absorption. According to Figure 5 and Table 2, the pterin ring has a dihedral angle of ϕ_1= 82.16 for the neutral model (C_{39}-N_{42}-C_{44}-C_{45}), a dihedral angle of ϕ_2 = 96.42 for the tumor model (C_{22}-N_1-C_{15}-C_{16}), and a narrow linear angle of ϕ_3 = 153.20 for the stomach pH model (C_{15}-N_1-C_{20}-C_{21}). This discovery leads us to conclude that the drug transport mechanism begins when the dihedral angle (ϕ) of the pterin ring becomes linear, while cell uptake is more favorable when it is perpendicular to the drug molecule.

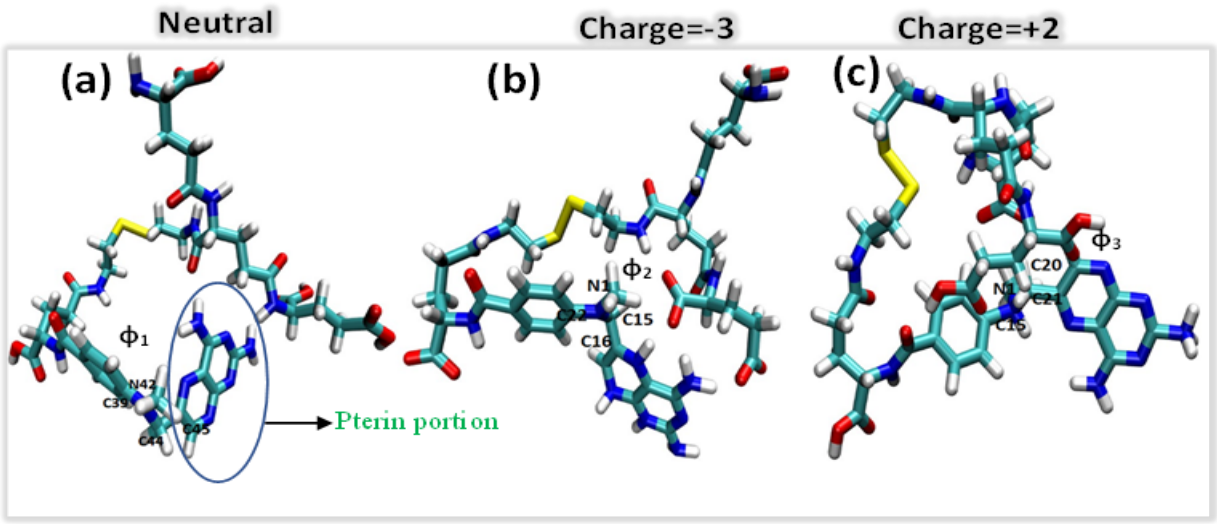

Figure 5: Geometry-optimized structural models of drug-loaded nanoparticles: (a) pH 7.0, (b) 6.4, and (c) 2.0. Reprinted (modified) with permission from source[141]; Copyright 2023 International Journal of Chemical Science.

Table 2. Charge and dihedral angles of the models (drug-loaded nanoparticles). With permission from source[141]; Copyright 2023 International Journal of Chemical Science.

pH	Charge	Dihedral angle (ϕ)
7.0	0	82.16
6.4	-3	96.42
2.0	+2	153.2

For the two complex structures from the simulation studies, POPC/MTX-SS-PGA (pH = 7) and POPC/MTX-SS-PGA (pH = 6.4), the coordinates were compared with the original reference structure. The RMSD deviation between the phosphate groups (PO_4^{3-}) of the membrane complexes at 303.15 K shows that both systems achieved an equilibrium of 1 ns to 30 ns in the simulation shown in Figure 6(a). In this case, the tumor model interacts

substantially with the lipid bilayer, which is proven by the fact that it is more stable than the neutral model. The RMSF analysis of the two complexes showed similar trends up to 30 ns (see Figure 6(b).

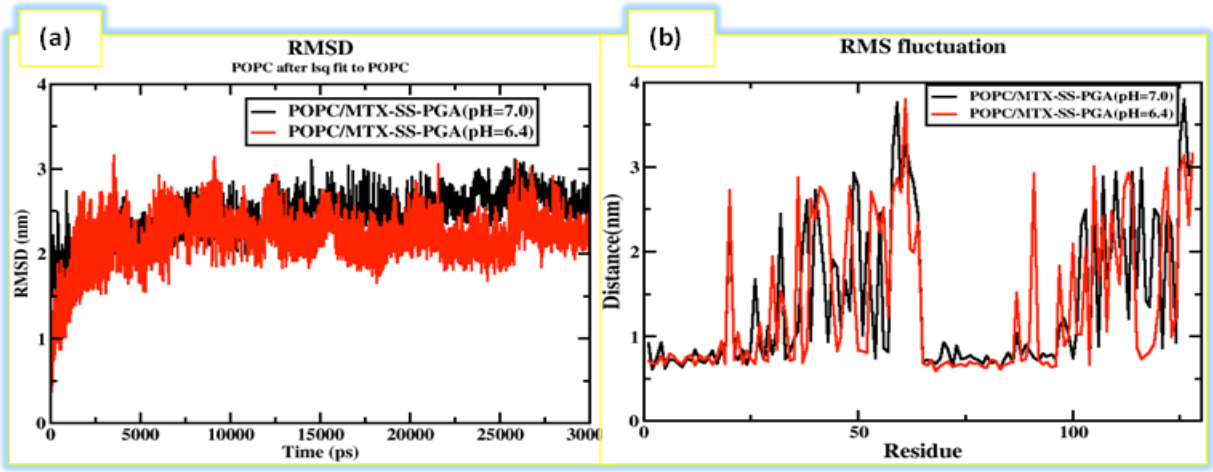

Figure 6(a). RMSD plot for both nanoparticles. **Figure 6(b)** shows the RMSF variation for the two nanoparticles. Reprinted (modified) with permission from source[141]; Copyright 2023 International Journal of Chemical Science.

The compactness of the lipid bilayer is measured by the area per lipid parameter, which is also used to assess whether the membrane is affected by an increase in penetration density. Report[142] states that the calculated APL of the pure membrane is 65.82 $Å^2$ and varies with temperature: 66$Å^2$at 310 K[143] and 62$Å^2$ at 310 K[144]. In our situation, I found that APL does not have much influence when comparing APL for the experimental POPC for two models of MTX-SS-PGA with pH values of 7.0 and 6.4 at 313.15 K and 63.94$Å^2$ and 63.89$Å^2$, respectively. For the third model, which has a pH of 2.0 and causes the system to become unstable[145], I was unable to determine the area per lipid, indicating that the drug delivery mechanism had begun. Compared to the POPC control, the density in both models was only slightly impaired, suggesting that our models had no significant effect on membrane density when they passed through the cell membrane. Quantifying the electron density profile by X-ray scattering of a liquid crystalline lipid membrane[146] can determine the thickness of the membrane. To calculate the electron density profile, the following formula is used: atomic number – the partial charge of electrons in the centre of an atom = electron charge. The density profile for POPC (1-palmitoyl-2-oleoyl-sn-glycerol-3-phosphocholine), phosphate (PO_4^{3-}), glycerol, water, MTX and the acyl chain. When comparing these two models, although both show a similar trend behaviour, in contrast to the tumor pH model, the density of the neutral phosphate group (PO_4^{3-}) is lower than 100

kg/ m^3. This is because the nanoparticles in the neutral model have less interaction with the cell membrane at the top, while in the model with a tumor pH (475 kg/m^3), this is because the pH range changes from neutral to turmeric (0 and -3 charge). In the other areas, such as MTX, acyl chain, POPC, and water, a fairly similar distribution was observed in both models.

Although this is a critical calculation of the PMF curve directly related to relative solubility, the membrane can be calculated from drug permeation studies in the solubility–diffusion compound. In our situation, I used two models of MTX-SS-PGA nanoparticles with different pH values; our goal was to estimate the permeation/cell uptake of drug-loading nanoparticles from the water phase to the membrane phase for the neutral and tumor model, as shown in Figure 7. When using the neutral model, the free energy barrier from the surface of the water through the polar head groups to the membrane was greater than the free energy barrier of the tumor model, as shown in Figure 7. Therefore, a pH of 7.0 is preferable to a pH of 6.4. Therefore, the tumor model favors penetration over the neutral model. Based on the inhomogeneous solubility diffusion[147] model developed with the help of the MD study, the permeation/cellular uptake of drug-loaded nanoparticles is one of the factors for the solubility of the molecule with water, hydrophobic lipid environment, free energy values, etc. Based on this assumption, the energy profile shows the concepts of a tumor model with depth energy minima compared to the neutral model. Although both drug-loaded nanoparticles have a depth energy profile at the lipid–bilayer interface, the passive transport mechanism appears to be a simpler inhomogeneous solubility diffusion model. I consider our quantitative comparison of our model with the experimental results to be a probable trend. I encountered several problems in the calculation of the barrier, particularly for the neutral pH model, because of the slow diffusivity of permeation through the lipid bilayer. Figure 7 clearly shows that both nanoparticles on the left side of the curve have a greater energy barrier due to the characterization of the permeation of nanoparticles into the hydrophobic tail of the bilayer core. Consequently, the energy of both nanoparticles decreased in the mass of the water phase. ΔG-free energy rises from the surface of the water into the interior of the membrane of the hydrophobic tail of the double-layer centre of mass (COM). The free energy profile indicates that neutral nanoparticles have a harder time penetrating the double layer than those with a pH value of the tumor. The increase in the density profile could be due to the difference in free energy. How does the density profile of different regions change as a result of different domains in different places? The density map of the head groups was not well reduced; this indicates

that the stronger interaction with the tumor model was easily taken by the cell membrane. As the model has a charge of -3, the density of the phosphate groups is not affected by the attraction of opposing charges (NH_4^+), which may explain why there is a stronger interaction with the lipid head groups. Instead, the amphiphilic properties of the nanoparticles caused the neural group to interact with the head groups. Consequently, the head groups of the density-energy profile of the neural form were significantly less affected than those of the tumor form. Furthermore, the geometry of the structure influences cell uptake, and as in our models, a more cage-like structure can penetrate the models without much resistance of the bilayer. Therefore, in the case of energy criteria, the penetration mechanism of nanoparticles from the aqueous phase into the interior of the membrane is also determined by energy. In this context, cell uptake can influence the charge, structure, and energy requirements of NPs for the drug or nanoparticles of bulk water to reach the interior of the membrane.

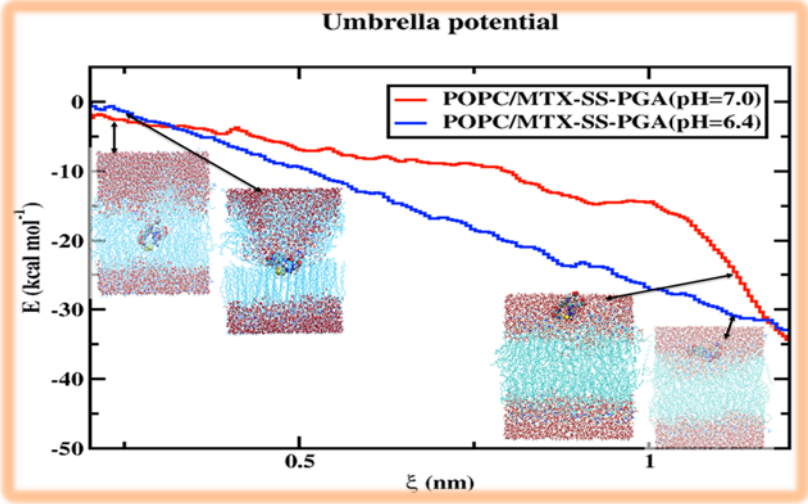

Figure 7. The free energy profile for the movement of a drug-loaded nanoparticle from the aqueous phase to the centre of the lipid bilayer. The interface of the lipid bilayer is represented together with the reaction coordinates from the centre-of-mass of the drug-loaded nanoparticle to the centre-of-mass of the lipid bilayer in the z-direction. Reprinted (modified) with permission from source[141]; Copyright 2023 International Journal of Chemical Science.

The tumor pH model penetrates the cell membrane significantly more quickly than the neutral model, although both models (neutral and tumor) have cage-shaped shapes. This is due to the distinct structure, charge, and energetics of the NP system. Due to this, the tumor model's hydrogen bond is higher than the neutral model's, indicating that this model has a greater solubility ratio. On the time axis, the average number of hydrogen bonds for tumor model was four, however, at a maximum of 8 h bonds at 300 ps. For the neutral model, the average number

of hydrogen bonds was three, with peaks of five occurring at 100 and 250 ps. The solubility and distance criteria for the phosphate and nitrogen atoms of a lipid bilayer with oxygen atoms of the nanoparticle describe the probability of finding one particle to another with a distance between r and r + dr, where the bond distance is deeper at the transition of the nanoparticle from the aqueous phase to the interior of the membrane. This RDF provides a singular description of the distance between two atoms, such as the "O" atom of the nanoparticle and the "P" and "N" atoms at the membrane interface. From these results, it is clear why there is a higher solubility and nanoparticle distance ratio with the head groups of the membrane (P and N atoms). This means that pH 6.4 (tumor) nanoparticles interact more strongly with the top layer of the head groups of the membrane than pH-neutral (7.0) nanoparticles. The enhanced penetrating power at the membrane interface is confirmed by the solubility ratio of the tumor pH nanoparticle, which is higher than the neutral one. In general, the solvation-free energy of an aqueous medium is significantly influenced by the magnitude of the dipole moment[148]. In our example, all three models have a significantly different magnitude of dipole moments on the basis of this supposition. For instance, the neutral and stomach pH models in Table 3 have dipole moments (Debye) of 5.3 D and 28.8 D, respectively, but the model for tumor pH has a dipole moment (Debye) that is substantially higher at 32.5 D. As a result of the interaction of high preferential dipole moments with the environment, larger dipole moments may have the potential for stronger free solvation energy in the aqueous phase. Because this solubility criterion is also a crucial element in determining cell uptake, it is assumed that the tumor pH model may have larger free solvation energies with water and thus be more stable when the cell membrane is. The stomach pH model, which is unstable due to the excessive acidity of medium[145], comes second, and the neutral model comes last.

Table 3. Lists the energy gap and dipole moment parameters for different models with permission from source[141]; Copyright 2023 International Journal of Chemical Science.

pH	Dipole moment (Debye)	Energy gap ($\Delta E_{H\text{-}L}$)
7.0	5.3	0.13 eV
6.4	32.5	0.06 eV
2.0	28.8	0.09V

In this study, I addressed the problem of drug-loaded functionalized nanoparticles being taken into cells, as predicted by MD simulations, and found that the neutral pH model made uptake more difficult than the tumor pH model. Based on the system, the charge, structure, and

energy of NP affect cellular uptake. However, the drug may be released in an acidic environment[145] according to the stomach pH model.

4.3. Case Study 3

The third part of my dissertation is presented in the publication "Core, coating, or corona? The importance of considering protein coronas in nano-QSPR modeling of zeta potential," which is **attached as publication [C]**. In this paper, I propose a machine learning-based model that describes the quantitative relationship between the structure of NPs defined by the so-called core and coating descriptors, their PC fingerprints in the biological medium defined by the so-called corona descriptors, and the nano-QSPR model with a value of zeta potential (ζ)-value nano-QSPR model. The Nano-QSPR model is based on partial regression of the least squares using a GA-PLS genetic algorithm characterized by high external predictive power Q^2_{EXT} = 0.89. The GA-PLS model was developed with descriptors that describe (i) the core structure determined by seven different types of polymer-based NM in the range of 20 different sizes, (ii) the coating structure with seven different functional groups, and (iii) 80 different protein compositions adsorbed on the surface of the NPs. The presented study is proof of the concept that the zeta potential of NPs can not only be modeled from the original structure of the NPs themselves but should be developed as both a function of the structural properties determined by the core and coating of the NPs and as a biological medium determined by the formation of the protein corona.

Methodology

For this model, 7 different types of polymers were used: polystyrene (PS), polylactic acid (PLA), polylactic acid-co-glycolic acid (PLGA), poly-ε-caprolactone (PCL), polyisobutyl-cyanoacrylate (PIBCA), poly-hexadecyl-cyanoacrylate (PHDCA), poly-glycidyl methacrylate (PGMA), and 7 different coatings with functional groups, such as carboxyl functions, amine functions, polyglycerol, PEG, dido-decyl-dimethyl-ammonium, dextran, and heparin. Surrounded by 80 different protein compositions, mainly fibrinogen, albumin, etc. Based on adsorption, proteins are considered binary values, where 1 means that adsorption is present, and 0 means that there is no adsorption. The data I obtained from the literature[149] focused on the variation of the zeta potential (ζ) [endpoint] to affect the data of the core, the coatings, and

the different protein compositions that play a crucial role in the system. For example, the protein adsorption ratio in the core and coatings was present at different nanoparticle particle sizes (nm) when the respective proteins were present or absent. The molecular structures of the polymer (core) and functional group (coating) were produced using the MOLDEN[150] software. Since I first produced all the polymers in dimer form, and the coatings (functionalization) are monomers, the remaining proteins are available in the form of protein fingerprints. Geometry optimization was performed for all collected molecular structures using the Gaussian 09 package[117] with the functionality of B3LYP using a 6-31G base set. The optimized molecular structures were confirmed by vibration analysis to ensure an energy-minimized structure without an imaginary frequency. Geometry optimization is useful for extracting the energy-minimized equilibrium conformation that allows full 3D parameters, such as WHIM, for descriptor calculations. To calculate the molecular descriptors for the nanomaterial consisting of cores, coatings, and proteins, I used the DRAGON[151] software. These comprise 148 descriptors, including 33 cores, 35 coatings and 80 different proteins. The data set was divided by increasing the order of the 20 endpoints (ζ) for the selected nanoparticle samples. Subsequently, the data set was divided into two types: the training set n = 14, the data for the development of the QSPR model, and the validation set k = 6, the data for external validation[152,153]. In this case, I used the most useful and least random method to divide our model into such a small data set that every third sample was included in the validation set (V). Furthermore, the first and last samples were randomly selected for the training set (T), while the second and penultimate samples were included in the validation set. This is because experience has shown that the first and last samples at this level have the greatest impact on the results of our model. Therefore, it is possible to maximize the scale of the model, which better predicts the prediction error of the most influential sample of compounds.

The QSPR model is based on a mathematical description of the physicochemical properties of molecular compounds (y), which always depend on variations in the molecular structure (X) of the given compounds. In this case, with the experimental data for only a few chemicals (y). It is always possible to predict the properties of unknown chemicals. The information obtained from the molecular descriptors (X) was calculated using a suitable regression approach for the entire group[154]. The PLS method is the standard algorithm used in many QSPR perspectives. The main advantage of this method is that it converts the original descriptor into latent vectors of LVs and uses latent vectors that are multicollinear with dependent and independent variables

for regression.[155] In this scenario, it is possible to compress the structural information into a smaller number of variables.[155] I used the most efficient genetic algorithm method (GA) to select the most relevant molecular descriptors for the PLS method. The GA was proposed by John Holland[156] to find a more comprehensive explanation and is a random search method to achieve optimized results. On the one hand, experimental data Y and, on the other hand, the matrix of molecular descriptors X were developed and validated: a QSPR model associated with the valuable gold standard principles of the Organization for Economic Cooperation and Development (OECD). In this study, the PLS approach was developed around 1975 using Herman Ward's QSPR model to model complex datasets[157]. The basic principle of the PLS study can be used by combining principal component analysis (PCA), correlation analysis (CA), and multiple linear regression MLR[158]. Unlike MLR, PLS can be used to analyze data that are highly collinear, noisy, and independently numerous X[159]. In our study, the relatively numerous collinear descriptors with different descriptors were difficult to describe. In PLS, the endpoint y_i of the zeta potential is described with various combinations of the previously automatically scaled main descriptors as independent variables x_1, x_2, x_3..., x_n, as indicated in Eq. 14.

$$y_i = b_0 + b_1x_1 + b_2x_2 + \ldots + b_nx_n \qquad (14)$$

Based on the best values (R^2) of the main descriptors extracted from the GA. To measure the goodness of fit of each model, the correlation coefficient (R^2, Eq. 15) and the root mean square calibration error (RMSEC, Eq. 16) were determined.

$$R^2 = 1 - \frac{\sum_{i=1}^{n}\left(y_i^{obs} - y_i^{pred}\right)^2}{\sum_{i=1}^{n}\left(y_i^{obs} - \tilde{y}_i^{obs}\right)^2} \qquad (15)$$

$$RMSEc = \sqrt{\frac{\sum_{i=1}^{n}(y_i^{obs} - y_i^{pred})^2}{n}} \qquad (16)$$

Where y_i^{obs} is the i-th compound of the observed experimental value of the property of the training set, y_i^{pred} is the i-th compound of the predicted value of the property of the training set, $\tilde{y}_{obs}$ is the mean experimental value of the property of the training set, and n is the number of

connections in the training set. To test this model, I checked the stability of sensitivity to the composition of the training set, for which I calculated the cross-validated coefficient Q^2_{LOO} (leave-one-out) method or the root mean square error of cross-validation (RMSECV). Both statistics were calculated according to Equations 17 and 18, which are presented below.

$$Q^2_{LOO} = 1 - \frac{\sum_{i=1}^{n} \left(y_i^{obs} - y_i^{predcv} \right)^2}{\sum_{i=1}^{n} \left(y_i^{obs} - \tilde{y}_i^{obs} \right)^2} \quad (17)$$

$$RMSECV = \sqrt{\frac{\sum_{i=1}^{n} (y_i^{obs} - y_i^{predcv})^2}{n}} \quad (18)$$

where y_i^{obs} is the i-th member of the observed experimental value of the characteristic of the training set, y_i^{predcv} is the predicted i-th member of the cross-validated value of the characteristic of the training set, $\tilde{y}^{obs}$ is the mean experimental value of the characteristic of the training set, and n is the number of members present in the training set. External cross-validation was expressed about the (Q^2_{EXT}) external cross-validation, and the root mean square error of prediction (RMSEP), as shown in Equations 19 and 20.

$$Q^2_{EXT} = 1 - \frac{\sum_{i=1}^{n} \left(y_i^{obs} - y_i^{pred} \right)^2}{\sum_{i=1}^{n} \left(y_i^{obs} - \hat{y}_i^{obs} \right)^2} \quad (19)$$

$$RMSEP = \sqrt{\frac{\sum_{j=1}^{n} (yi^{obs} - yi^{pred})^2}{k}} \quad (20)$$

While y_i^{obs} is the i-th compound of the observed experimental value of the property from the training set, y_i^{pred} is the i-th compound of the predicted value of the property from the

validation set, $\hat{y}^{obs}$ is the mean experimental value of the property from the validation set, and k is the number of connections in the validation set. The Williams plot consists of standardised residuals versus levers used to verify and visualise the scope AD of the QSPR models. According to this formula: $h_i = X_i^T (X^T X)$, the levered value "h" for the i-th compound represents the distance of the chemical structure of this compound from the model. If the compound is included in the training set, a high leverage value (h) can strengthen the model. The leverage value of the new predicted compound indicates whether the compound has been interpolated or whether the results have been extrapolated. If the chemical value $h > h^*$ is critical, where $h^* = 3\ p\ n^{-1}$, where p is the number of variables plus one and n is the number of compounds in the training set. This means that the model is extrapolated when the predicted Y outcomes are out of range, i.e., in the case of interpolation, when $h < h^*$, if the model of the chemical's predicted Y outcomes is less reliable than other predictions[160]. This approach makes it easy to visualize both the outliers and/or compounds with high leverage and to standardize the remaining units that are greater than 3 standard deviation units.

Results and Discussion

The application of GA-PLS is to find the best combination of descriptors based on the R^2 Score. Descriptors, such as average molecular weight (core), nCsp2 (coatings), complementary subcomponent C1r, Apo A-I, and kininogen-1 (proteins), were determined. The final PLS model Eq. 21 was developed based on the 5 descriptors consisting of two latent vectors LVs.

$$\zeta = -7.857 + [16.228]\ \mathbf{AMW\text{-}P}_{\mathbf{Core\_desc}} + [-\ 9.559]\ \mathrm{nCsp2} - \mathbf{C}_{\mathbf{Coating\_desc}} + [21.720]\ \mathbf{CC1rs}_{\mathbf{Corona\_desc}} + [17.520]\ \mathbf{AA\text{-}I}_{\mathbf{Corona\_desc}} + [-5.392]\ \mathbf{kininogen\text{-}1}_{\mathbf{Corona\_desc}} \quad (21)$$

The R^2 for the training set was 0.957 (LV1 = 83%, LV2 = 12.5%) of the total variance in the X matrix and the Y vector, the Q^2 value for the validation set was 0.894 (LV1 = 53.1%, LV2 = 36.1%) of the covariance, and the root-means square error calibration was RMSEC = 6.832. The cross-validated (leave-one-out) correlation coefficient was $Q^2_{cv} = 0.442$, with RMSECV = 24.509. These values are indicative of the robustness of our model. The predictive power of the value was also satisfied by the value of $Q^2_{EXT} = 0.894$, $RMSE_P = 7.331$; there was a good correlation between the observed and predicted values (cross-validated values over a training set) in Figure 8.

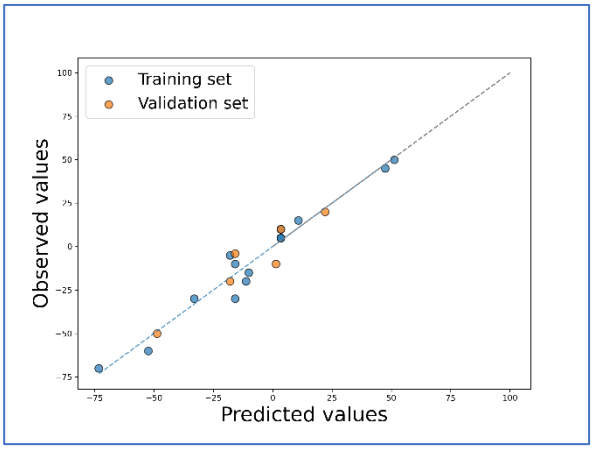

Figure 8. A plot of experimentally observed versus predicted values of zeta potential for training and validation compounds for QSPR models. Reprinted (modified) with permission from source[c]; Copyright 2023 American Chemical Society.

Looking at the Williams plot (Figure 9).), there were no values greater than the residual value of 2.5 in the training and validation sets of the compounds, with a leverage value of h^* =1.07, and all leverage values of the compounds are lower than the critical value (h^*). This shows that the values are within the common range of application (AD).

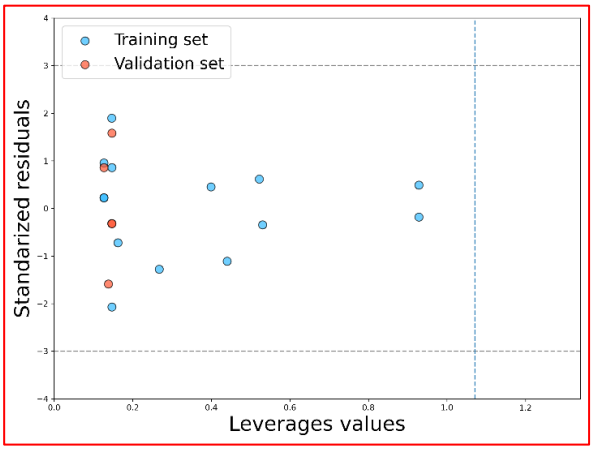

Figure 9. Williams diagrams for the QSPR model. Reprinted (modified) with permission from source[c]; Copyright 2023 American Chemical Society.

If we consider the latent distribution of LV1 values under normal load, I get a value range of -0.348, -0.108, and 0.578, such as the complement C1r subcomponent, Apo A-I, and kininogen-1 (proteins), nCsp2 (coatings) for 0.656, and AMW (core) for -0.379. The values clearly show that LV1 has a positive (+ve) and negative (-ve) distribution of latent vectors

among the 148 descriptors, 3 of which are only for proteins and the remaining 2 for the core and coatings.

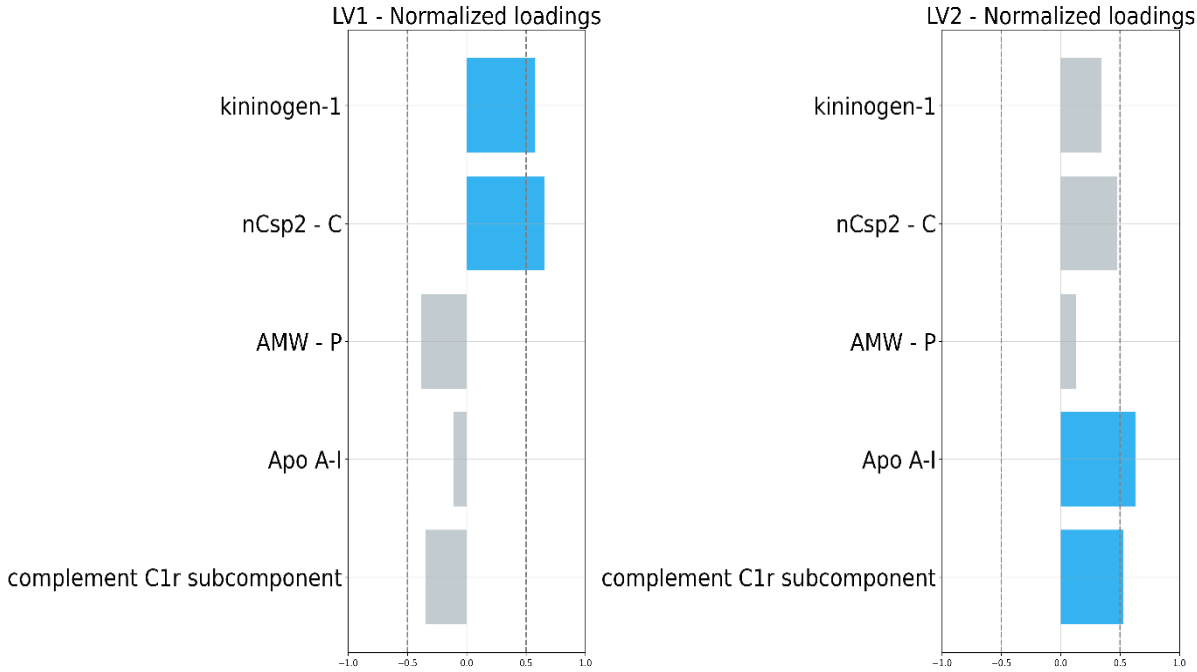

Figure 10. Loading values of individual latent vectors (LVs). Reprinted (modified) with permission from source[c]; Copyright 2023 American Chemical Society.

The distribution of LV1 shows that proteins and coatings are more distributed in latent space than in the core, but in LV2 in Figure 10, there is a positive side distribution (+ve) only in latent space; the higher distribution is 0.529, 0.630, and 0.340 only for proteins, 0.474 for coatings, and 0.127 for the core. Furthermore, the model equation shows higher coefficient values of 21,720 cC1r, 17,520 AA-I, and -5,392 k-1, which are available only for proteins. In this context, all indications indicate that the zeta potential is influenced not only by the core and coatings, but also by the fact that proteins play an important role in the mechanisms that influence the zeta potential, which confirms our model[161].

According to the usual criteria, solutions with a zeta potential are very stable in the range $\zeta < -30$ mV or $> +30$ mV[162]. If the values of the zeta potential (ζ) tend toward 0, the possibility of dispersion is very limited, which leads to the phenomenon of agglomeration/aggregation occurring easily. In our case, of the 20 samples, 15 were PS_CF_2, PS_Pol, PCL_D_5, PHDCA_PEG, PIBCA_DC, PS_CF_3, PCL_PEG, PCL_D_40, PS_CF_1, PS_AF_1, PS_AF_4, PS_AF_3, PS_AF_5, PLGA_DA_2, and PGMA_PEG, with values close to $\zeta > \pm 30$ mV from the obtained zeta potentials (ζ) from -70 mV to + 50 mV. However, in the case of

the sample, the combination PS-NH_2 has the most positive zeta potential ζ= + 50 mV. Similarly, PLGA-dido-decyl-dimethylammonium has a zeta potential of ζ = +45 mV. I hypothesize that these two compounds are likely to absorb cells due to the stronger cationic surface charge of NP than the anionic surface charge NP, which has the electron-donating property of the amino group (NH_2) due to the combination of PS-NH_2, which is a positively charged NP (+ve). In this scenario, cells would absorb more cationally charged NP than others, similar to this combination of PLGA-Dido-Decyl-Dimethylammonium; this phenomenon is strongly correlated with experimental data[163]. Based on the value of ζ, I can speculate that the functional group of coatings plays an important role in influencing the structure and properties of NPs, among other things. This influences the ζ[164] based on these values; nanoparticles coated with acidic functional groups are in the range of negative zeta potential, and vice versa, those with basic functional groups in the range of positive zeta potential. In our case, the combination of PS_CF1 (150 nm) nanoparticles has a higher mode than others in terms of protein adsorption, while a similar combination of PS_CF2 (130 nm) and PS_CF2 (140 nm) compounds has lower surface adsorption because this combination of nanoparticles (PS_CF1) has a larger surface area relative to the volume of higher order, according to a recent report[165]. However, the idea of a negative zeta potential (-4 for PS_CF1), which can adsorb proteins that occasionally have very little or no absorption and are still a mystery[166] in our situation, is controversial. Due to their charge[167] and numerous interactions, the combination of PS_AF-functionalized nanoparticles contributes to the second-and third-largest protein adsorption. PCL_D_40 and PGMA_PEG nanoparticles cause protein adsorption backward due to their more complicated structure.

The FPs in the study encode the structural data contained in the molecules as a bit vector. They consist of a series of bits, with a bit with a value of 0, indicating the absence of a structural protein property at this point. A bit with a value of 1 indicates the presence of a protein in a particular molecular property. CC1rs, the original descriptor specified in the constructed model as serine protease (Eq. 21), showed that the presence of serine protease influenced the zeta potential of the investigated PNP. Data [168(d)] show that CC1r describes the stability of coated NPs. Furthermore, the experimental results of Donald et al[169] clearly show that the presence of lipase and protease treatment did not restore the reactivity of coated NP. Corona-coated NPs are stable when functionalized in the presence of lipase and protease and prevent hemolytic activity and membrane deterioration when intact[168(d)]. In the constructed nano-QSPR model

(Eq. 21), the second corona descriptor was associated with the alpha-amylase inhibitor (AA-I). Interestingly, a previous study by Sreeram et al.[168(a)] showed that the kinetic analysis showed that the presence of protease in an enzyme medium influences the biological activity of amylase, as evidenced by the decrease in the amylase values of K_m and V_{max}. Amylase is not denatured when the enzyme is immobilized in CuO-NP and has a high affinity for CuO[168(a)] NP. In other words, the stability of the NPs resulted from the biofunctionalization of the CuO-NPs with the protease-amylase complex. Kininogen-1 expresses the third corona descriptor used in the Nano-QSPR model. Superparamagnetic iron oxide nanoparticles (SPION) with two different polyvinyl alcohol polymers (PVA) and dextran (DX) were used in the study by Sakulkhu et al.[170], which showed that proteins such as kininogen-1 were positively, negatively, and neutrally adsorbed in NP regardless of the type of material and surface charge. However, the authors discovered that PVA-coated SPIONs with negative and neutral surface charges absorbed more serum proteins than DX-coated SPIONs, resulting in a longer blood circulation time for PVA-coated NPs than for DX-coated Ones[171]. Finally, the core and coating descriptors of the constructed nano-QSPR model in Equation 21 clearly show a correlation between the zeta potential and the size of the PNPs. Their results are consistent with those published in the literature[77,172]. Therefore, the results of Yallapu et al[173] showed that there was no discernible change in the particle size of the NPs after incubation of the investigated NPs with human serum (HS). Due to human serum[174], the zeta potential of NP changed simultaneously. Furthermore, C4-2B and Panic-1 cancer cells showed increased internalization and uptake of NP after incubation with human serum (HS).

In summary, the study presented here shows that not only the functionalized NP itself but also the original structure can be used to simulate the zeta potential of PNP. From the engineered nano-QSPR model (Eq. 21), it is clear that the zeta potential should be represented both as a function of the structural features determined by the core and coating and as a biological medium formed by the corona formation of the protein (Eq. 21). Machine learning models are expected to control and/or shape the stability of NPs in a particular medium.

4.4. Case Study 4

The fourth part of my dissertation is presented in the paper "Rapid colorimetric discrimination of cyanide ions - mechanistic insights and applications" (**attached as**

publication [D]). In this paper, I propose how the colorimetric response of the transition to the malononitrile-functionalized DMN probe prevents intramolecular charge transfer when cyanide ions are added, leading to the development of a Michael adduct at the site where the dicyanovinyl group is cyanide β-conjugated. Rapid colorimetric detection of dangerous ions from samples is another difficult task; based on the problem of interest, we have worked with an intramolecular charge-based functionalized DMN probe with cyanide ion (CN^-) detection from many samples or water samples using the naked eye. In this context, computational and spectroscopic methods were used for the intermolecular interaction of the functionalized DMN probe with cyanide ions in the investigated solutions. In this case, we used a TD-DFT calculation to calculate the absorption spectra for these probes, and our results correlated well with the experimental data using an additional molecular electrostatic potential (MESP) map to understand the mechanism of charge variation of the nucleophilic addition of cyanide ions inside and outside the detector. Accordingly, the colorimetric detection mechanism of functionalized DMN in cyanide ions was established, which was validated with a paper-based microfluidic device that could easily detect cyanide ions in a lower-concentration solution. In addition, an open-source Android application and a portable 3D-printed smartphone accessory that can be used with the malononitrile-functionalized DMN probe for fieldwork have been developed. In addition, we have developed a paper-based microfluidic analyzer with a colorimetric functionalized DMN probe that can selectively detect cyanide ions at very low concentrations.

Methodology

The Truhlar functional approach M06-2X/6-31G and the Gaussian 09 package were used to calculate the geometry optimization of the malononitrile-functionalized DMN probe and the cyanide.[117] The frequency calculations, which did not correspond to a negative imaginary frequency, allowed confirmation of the ultimately optimized geometry. To calculate the absorption spectra of the probe using the TD-DFT method, I used a variety of functionals, B3LYP, BP86, CAM-B3LYP, M06-2X, B3P86, and PBE, as well as the basis sets 6-31G, 6-31+G, 6-31+G* and 6-311+G. λ_{max} value with empirical data for DMN, as the absorption spectrum produced has a large overlap with the experimental absorption spectrum in THF solvents. To account for the solvent environment around the molecules, SCRF-PCM-based M06-2X was functionally integrated with a 6-31G base set used for TD-DFT calculations.

The time-dependent density functional theory is expressed in the Kohn-Sham diagram and states that only the originally occupied "N" orbitals are multiplied. How can this be sufficient to take into account all possible excitation processes? Here is a brief explanation:

Complete extension of TDKS orbitals in the context of KS orbitals in Equation 22.

$$\phi_j(r, t) = \sum_{k=1}^{\infty} a_{jk}(t)\, \phi_k^{(0)}(r) \quad (22)$$

finite for k > N

Due to its time-dependent potential, TDKS orbitals receive admixtures from originally unoccupied orbitals.

Results and Discussion

Calculations of density functional theory (DFT) for DMN and cyanide anions at the M06-2X/6-31G level were carried out using the Gaussian 09 program. The dihedral angles of the atoms in the DMN structures that have been optimized are C_8-N_7-C_{27}-C_{32} and C_8-N_7-C_2-C_1, where $\phi_1 = -50^o$ and $\phi_2 = 50^o$ respectively. Accordingly, the malononitrile-functionalized DMN is a non-planar structure, and the two phenyl rings are twisted out of the plane. However, after interaction with the cyanide ion, the dihedral angles ϕ_1 and ϕ_2 were changed to -44.4° and -46.5°, respectively. In contrast, the planar character of the acceptor is also cancelled ($\phi_3 = -126.45^o$ and $\phi_4 = 55.53^o$). This perturbation weakens the strength of the ICT character of DMN, resulting in a significant blue shift in the absorption spectrum. In the ditolyl aminothienyl group, the electron density of DMN is centred at HOMO. However, LUMO is mainly concentrated in the dicyanovinyl group, indicating an ICT from the ditolyl-aminothienyl group to the dicyanovinyl group (Figure 11). In the presence of cyanide anions, the LUMO is restricted to the benzothiadiazole groups because the ICT process is slowed down. As a result, a blue shift was observed in the absorption spectra, confirming the calculation results and experimental findings.

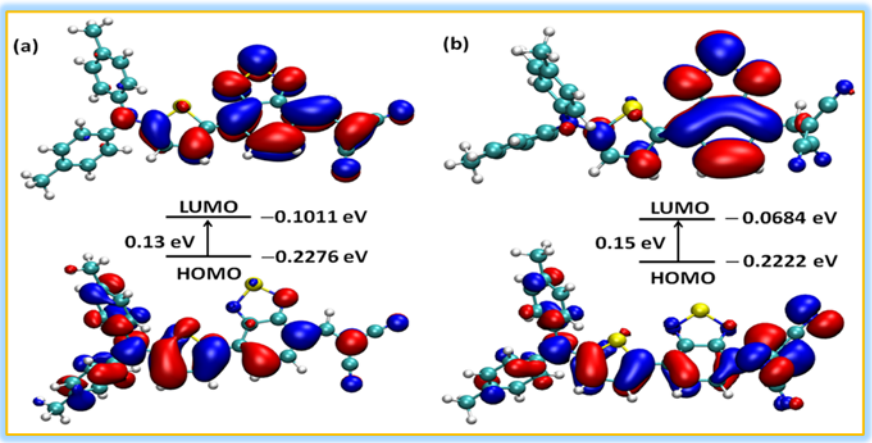

Figure 11. HOMO-LUMO diagram of (a) the DMN probe and (b) the cyanide ion. Reprinted (modified) with permission from source[175]; Copyright 2022 by the Royal Chemical Society.

How the charges are distributed in a molecular assembly can be better understood using the example of the molecular electrostatic potential (MESP). In this case, it is much more helpful to visualize the charge distribution when a foreign molecule is present. MESP analyses were performed to determine how the malononitrile-functionalized DMN probe and cyanide ions interacted under these circumstances. The MESP color diagram for DMN and DMN+CN^- is shown. Red and blue are often used to indicate whether an electron is present in a molecule. However, the functionalized DMN probe in Figure 12 shows that the acceptor moiety is essentially neutral. This study shows that nucleophilic addition, when the cyanide ion is bound to the dicyanovinyl moiety, prevents conjugation of triphenylamine and the dicyanovinyl moiety. The experimental results confirm this conclusion.

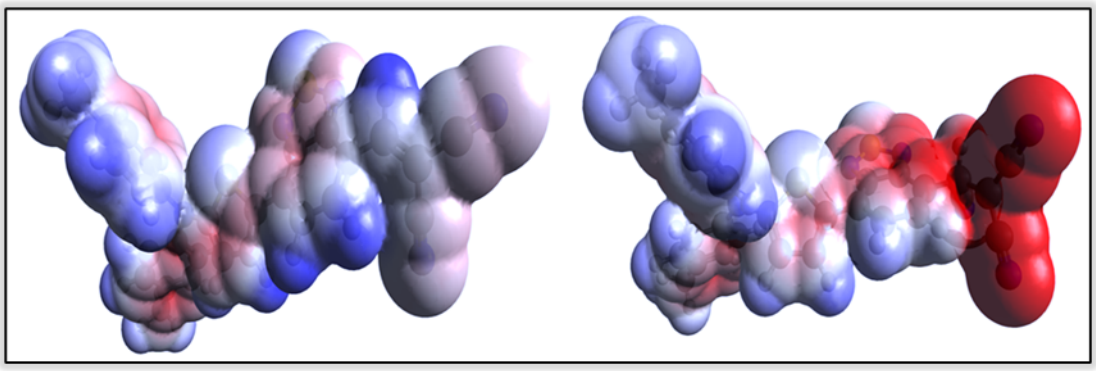

Figure 12. Map of the molecular electrostatic potential of DMN and cyanide ions (right). Reprinted (modified) with permission from source[175]; Copyright 2022 by the Royal Chemical Society.

When the properties of the malononitrile-functionalized DMN probe are calculated, a different functional set and a different basis set are used to calculate the absorption spectra. The absorption spectra calculated by us correspond well to the experimental spectral studies; the values are listed in Table 4.

Table 4. λ_{max} values calculated for the functionalized DMN probe based on different functional and basis sets at 645 nm are the experimental λ_{max} value. With permission from source[175]; Copyright 2022, Royal Chemical Society.

Functional	Basis set	λ_{max} (nm)
B3LYP	6-31G	663
	6-31+G	681
	6-31+G*	622
	6-311G	661
	6-311+G	673
BP86	6-31G	874
CAM-B3LYP	6-311G	618
M06-2X	6-31G	635
B3P86	6-31G	740
PBE	6-31G	870

In summary, an ICT-based malononitrile-functionalized DMN probe was used for the fast colorimetric detection of cyanide ions in solution with the help of computer studies. Because the functionalized DMN probe is based on the ICT channel, its special properties enable fast and accurate detection. Ditolylaminothienyl and dicyanovinylene were separated by a

nucleophilic attack of the cyanide ion, which closed the ICT channel and caused colorimetric changes. DFT studies were able to locate the cyanide ion sensor mechanism. To understand how the malononitrile-functionalized DMN probe and cyanide ions interact, I conducted an MESP study.

5. Conclusions and future perspectives

In my dissertation, I describe the application of newly functionalized material preparations in real life. Our strategic modeling approach will help to design new compounds. The ultimate goal of our study was to improve the functions and properties of our compounds compared to those of previous compounds in their applications. In conclusion, I modeled newly effective Schiff-based functionalized pyrene derivatives that were mainly effective against antibacterial infections compared to similar compounds. I also developed a functionalized probe that could easily detect cyanide CN^- from a variety of water samples. Our modeling method could be useful for extracting toxic ions very quickly. Later, I turned to nanoscale projects that focused mainly on characterizing the physicochemical properties of functionalized nanoparticles with our nano-QSPR method, as in the case of nanoparticles in the blood, where the proteins on the surface of the nanoparticles are adsorbed, especially the albumins and globulins, as shown in the experimental report. Therefore, we focused on the proteins covered by the nanoparticles, which led to the formation of a protein corona. This protein corona influences the physicochemical properties of the zeta potential, which vary for different types of nanoparticles, as this surface charge or zeta potential is a very influential factor in the cell uptake and toxicity of the materials. Furthermore, I have worked on the drug delivery mechanism of drug-loaded functionalized nanoparticles with variable criteria that influence cell uptake mechanisms at different pH levels, such as neutral, tumor, and stomach pH ranges of 7.0, 6.4, and 2.0. In this work, I explain how the effects of the charge, geometry, and energetics of functionalized NPs affect cell uptake at different pH values. Based on these facts, I observed that the pH range of the stomach of nanoparticles, which destabilized the system by a more acidic medium, led to the delivery of the drug through the mechanism of glutathione attacking the disulfide bond and releasing the drug at the exact site, based on the experimental evidence and the short uptake of the tumor than the neutral pH model.

Based on the above conclusion, we hypothesized that our studies could help to develop new compounds with different perspectives when they interact with plasma proteins and that the developed material would be able to detect harmful ions with the naked eye. Our Nano-QSPR method is the first attempt to test the zeta potential of untested chemicals. Based on the mechanism of drug delivery, our method could help to develop new drug-loaded functionalized nanoparticles to improve drug development and delivery.

I hope that my study will be useful in the search for new functional materials, from organic molecules to nanoscale materials, by using different and reliable computer tools to predict new properties with improved efficiency factors in both organic and nanoscale materials.

In summary, I have developed a sequential approach to computer tools, that predicts new functional materials that are useful for the most important human applications in daily life, including the fact that the nano-QSPR method based on machine learning helps predict the zeta potential of untested compounds.

As an extension of our work, there is the possibility of establishing a valuable protocol for screening drug molecules based on free-energy binding values to proteins and the analysis of energy gaps, leading to the discovery of potential drug molecules that more strongly influence our expected properties.

Second, I have developed new materials using a cost-effective method that can detect not only ions but also toxic metal ions, which helps remove heavy metal ions from the sample from an ecological point of view.

Third, my next goal is to work on PC influences on the physicochemical characterization of nanomaterials. In particular, I will focus on pH and how pH is affected when functionalized nanomaterials are present in the human body. Finally, I will develop new drug-loaded functionalized nanoparticles that are less toxic and have lower concentrations to increase the effectiveness of the drug and use our model to improve drug delivery based on various criteria, along with the methodology of drug development.

6. REFERENCES

1. Leroy G. Wade, Jr. Organic Chemistry, Pearson Prentice Hall, Upper Saddle River, NJ, 4th edition. 1998.
2. Kitadai, Norio, and Shigenori Maruyama. Origins of building blocks of life: A review. *Geoscience Frontiers.* 2018, 9, 1117-1153.
3. CLARKE, S. Organic chemistry. Essential Chemistry for Aromatherapy. 2008, 25–40.
4. Lombardo, Domenico, Pietro Calandra, Luigi Pasqua, and Salvatore Magazù. Self-assembly of organic nanomaterials and biomaterials: the bottom-up approach for functional nanostructures formation and advanced applications. *Materials.* 2020, 13, 1048.
5. Cheng, Tsai-Mu, Hsiu-Yi Chu, Haw-Ming Huang, Zi-Lin Li, Chiang-Ying Chen, Ya-Jung Shih, Jacqueline Whang-Peng et al. Toxicologic Concerns with Current Medical Nanoparticles. *Internat. J. Mol. Sci.* 2022, 23, 7597.
6. Babanli, M. B., F. Prima, P. Vermaut, L. D. Demchenko, A. N. Titenko, S. S. Huseynov, R. J. Hajiyev, and V. M. Huseynov. Review on the new materials design methods. In International Conference on Theory and Applications of Fuzzy Systems and Soft Computing, Springer, Cham. 2018, 937-944.
7. Ravoof, Thahira BSA, Karen A. Crouse, M. Ibrahim M. Tahir, Fiona NF How, Rozita Rosli, and David J. Watkins. Synthesis, characterization, and biological activities of 3-methylbenzyl 2-(6-methyl pyridin-2-ylmethylene) hydrazine carbodithioate and its transition metal complexes. *Transit. Met. Chem*. 2010, 35, 871-876.
8. How, Fiona N-F., Karen A. Crouse, M. Ibrahim M. Tahir, M. T. H. Tarafder, and Andrew R. Cowley. Synthesis, characterization, and biological studies of S-benzyl-β-N-(benzoyl) dithiocarbazate and its metal complexes. *Polyhedron* 2008, 27, 3325-3329.
9. Manan, Mohd Abdul Fatah Abdul, M. Ibrahim M. Tahir, Karen A. Crouse, Rozita Rosli, Fiona N-F. How, and David J. Watkin. The crystal structure and cytotoxicity of centrosymmetric copper (II) complex derived from S-methyldithiocarbazate with isatin. *J. Chem. Crystallogr*. 2011, 41, 1866-1871.

10. Jasinski, Jerry P., Jason R. Bianchani, Juan Cueva, Fathy A. El-Saied, Ahmed A. El-Asmy, and Douglas X. West. Spectral and Structural Studies of the Copper (II) Complexes of 3, 4-Hexanedione Bis (3-azacyclothiosemicarbazones). *Z. Anorg. Allg. Chem.* 2003, 629, 202-206.
11. Hassan, A.S.; Askar, A.A.; Nossier, E.S.; Naglah, A.M.; Moustafa, G.O.; Al-Omar, M.A. Antibacterial evaluation, in silico characters and molecular docking of Schiff bases derived from 5-aminopyrazoles. *Molecules.* 2019, 24, 3130.
12. Gümüs, A.; Okumus, V.; Gümüs ¸S. Synthesis, biological evaluation of antioxidant-antibacterial activities and computational studies of novel anthracene-and pyrene-based Schiff base derivatives. *Turk. J. Chem.* 2020, 44, 1200–1215.
13. Erturk, A.G. Synthesis, structural identifications of bioactive two novel Schiff bases. *J. Mol. Struct.* 2020, 1202, 27299.
14. Mishra, N.; Kumar, K.; Pandey, H.; Anand, S.R.; Yadav, R.; Srivastava, S.P.; Pandey, R. Synthesis, characterization, optical and anti-bacterial properties of benzothiazole Schiff bases and their lanthanide (III)complexes. *J. Saudi Chem. Soc.* 2020, 24, 925–933.
15. Srinivasan, V.; Khamrang, T.; Ponraj, C.; Saravanan, D.; Yamini, R.; Bera, S.; Jhonsi, M.A. Pyrene based Schiff bases: Synthesis, crystal structure, antibacterial and BSA binding studies. *J. Mol. Struct.* 2021, 1225, 129153.
16. Prasad, Honnegowdanahalli Shivabasappa Nagendra, Navyatha Prashanth Gaonkar, Agasanapura Puttaswamy Ananda, Amogh Mukarambi, Guddappa Charan Kumar, Tumakuru Nagarajappa Lohith, and N. Beeregowda. Antibacterial Property of Schiff-based Piperazine against MRSA: Design, Synthesis, Molecular Docking, and DFT Computational Studies. *Lett. Appl. NanoBioSci.* 2022, 2, 54.
17. Kathiravan, Arunkumar, Karuppasamy Sundaravel, Madhavan Jaccob, Ganesan Dhinagaran, Angappan Rameshkumar, Devanesan Arul Ananth, and Thilagar Sivasudha. Pyrene Schiff base: photophysics, aggregation induced emission, and antimicrobial properties. *J. Phys. Chem. B.* 2014, 118, 13573-13581.
18. Zhang, Wenjie, Reza Taheri-Ledari, Fatemeh Ganjali, Fereshte Hasanzadeh Afruzi, Zoleikha Hajizadeh, Mahdi Saeidirad, Fateme Sadat Qazi et al. Nanoscale Bioconjugates: A review of the structural attributes of drug-loaded nanocarrier conjugates for selective cancer therapy. *Heliyon*, 2022, 8, e09577.

19. Roberts GCK, Feeney J, Birdsall B, et al. Methotrexate binding to dihydrofolate reductase. *Nature* 1980, 286, 309.
20. Li Y, Lin J, Ma J, et al. Methotrexate-camptothecin prodrug nano assemblies as a versatile nanoplatform for biomodal imaging-guided self-active targeted and synergistic chemotherapy. *ACS Appl. Mater. Interfaces* 2017, 9, 34650–34665.
21. Li S, Yuan S, Zhao Q, et al. Quercetin enhances chemotherapeutic effect of doxorubicin against human breast cancer cells while reducing toxic side effects of it. *Biomed. Pharmacother.* 2018,100, 441–447.
22. Shi J, Kantoff PW, Wooster R, et al. Cancer nanomedicine: progress, challenges and opportunities. *Nat. Rev. Cancer.* 2017, 17, 20–37.
23. Mou Q, Ma Y, Zhu X, et al. A small molecule nanodrug consisting of amphiphilic targeting ligand–motherapy drug conjugate for targeted cancer therapy. *J. Control. Release.* 2016, 230, 34–44.
24. Rajabi A, Aieneravaie M, Dorosti V, et al. Development and biomedical application of nanocomposites: in situ fabrication of ZnO–PbO composite through microwave method. *Mater. Technol.* 2014, 29, 227–231.
25. Karve S, Werner ME, Sukumar R, et al. Revival of the abandoned therapeutic wortmannin by nanoparticle drug delivery. *Proc. Natl. Acad. Sci. U.S.A.* 2012, 109, 8230–8235.
26. Van De Waterbeemd H, Smith DA, Beaumont K, et al. Property-based design: optimization of drug absorption and pharmacokinetics. *J. Med. Chem.* 2001, 44,1313–1333.
27. Maeda H. Toward a full understanding of the EPR effect in primary and metastatic tumors as well as issues related to its heterogeneity. *Adv. Drug. Deliv. Rev.* 2015, 91, 3–6.
28. Maeda H. Macromolecular therapeutics in cancer treatment: the EPR effect and beyond. *J. Control. Release* 2012, 164,138–144.
29. Maeda H, Nakamura H, Fang J. The EPR effect for macromolecular drug delivery to solid tumors: improvement of tumor uptake, lowering of systemic toxicity, and distinct tumor imaging in vivo. *Adv. Drug. Deliv. Rev.* 2013, 65, 71–79.
30. Wilhelm S, Tavares AJ, Dai Q, et al. Analysis of nanoparticle delivery to tumours. *Nat. Rev. Mater.* 2016, 1, 16014.

31. Bertrand N, Wu J, Xu X, et al. Cancer nanotechnology: the impact of passive and active targeting in the era of modern cancer biology. *Adv. Drug. Deliv. Rev.* 2014, 66, 2–25.
32. Sonar YA, Mahajan HS. Development of glucosamine functionalized micelles as a potential drug delivery system for targeting to brain. *Mater. Technol.* 2019, 35, 1–9.
33. Theek B, Gremse F, Kunjachan S, et al. Characterizing EPR-mediated passive drug targeting using contrast-enhanced functional ultrasound imaging. *J. Control. Release.* 2014,182, 83–89.
34. Bao W, Ma H, Wang N, et al. pH-responsive mesoporous silica drug delivery system for targeted cancer chemotherapy. *Mater. Technol.* 2020, 1–9
35. Xu C, He W, Lv Y, et al. Self-assembled nanoparticles from hyaluronic acid-paclitaxel prodrugs for direct cytosolic delivery and enhanced antitumor activity. *Int. J. Pharm.* 2015, 493, 172–181.
36. Guo Q, Kong F, Ma C, et al. Preparation of doxorubicin loaded Poly (ethylene glycol)-Poly (ε- caprolactone)-hydroxyapatite fibres as drug delivery systems. *Mater. Technol.* 2020, 35, 203–211.
37. Li Y, Liu G, Ma J, et al. Chemotherapeutic drug-photothermal agent co-self-assembling nanoparticles for near-infrared fluorescence and photoacoustic dual-modal imaging-guided chemo-photothermal synergistic therapy. *J. Control. Release.* 2017, 258, 95–107.
38. Riehemann K, Schneider SW, Luger TA, et al. Nanomedicine–challenge and perspectives. *Angew. Chem.* 2009, 48, 872–897.
39. Lammers T, Kiessling F, Hennink WE, et al. Drug targeting to tumors: principles, pitfalls and (pre-) clinical progress. *J. Control. Release.* 2012, 161, 75–187.
40. Jain RK, Stylianopoulos T. Delivering nanomedicine to solid tumors. *Nat. Rev. Clin. Oncol.* 2010, 7, 653–664.
41. Aferni, A.E.; Guettari, M.; Tajouri, T.; Rahdar, A. The confinement of PVP in AOT microemulsions: Effect of water content and PVP concentration regime on electrical percolation phenomenon. *J. Mol. Liq.* 2020, 318, 114012.
42. Fytianos, G.; Rahdar, A.; Kyzas, G.Z. Nanomaterials in cosmetics: Recent updates. *J. Nanomater.* 2020, 10, 979.

43. Hakami, T.M.; Davarpanah, A.; Rahdar, A.; Barrett, S. Structural and magnetic study and cytotoxicity evaluation of tetrametallic nanoparticles of $Co_{0.5}Ni_{0.5}Cr_xFe_{2-x}O_4$ prepared by co-precipitation. *J. Mol. Struct.* 2018, 1165, 344–348.
44. Hasanein, P.; Rahdar, A.; Bahabadi, S.E.; Kumar, A.; Kyzas, G.Z. Manganese/cerium nanoferrites: Synthesis and toxicological effects by intraperitoneal administration in rats. *Inorg. Chem. Commun.* 2021, 125, 108433.
45. Heydari, M.; Yousefi, A.R.; Rahdar, A.; Nikfarjam, N.; Jamshidi, K.; Bilal, M.; Taboada, P. Microemulsions of tribenuron-methyl using Pluronic F127: Physico-chemical characterization and efficiency on wheat weed. *J. Mol. Liq.* 2021, 326, 115263.
46. Rahdar, A.; Aliahmad, M.; Samani, M.; HeidariMajd, M.; Susan, M.A.B.H. Synthesis and characterization of highly efficacious Fe-doped ceria nanoparticles for cytotoxic and antifungal activity. *Ceram. Int.* 2019, 45, 7950–7955.
47. Salimi, A.; Zadeh, B.S.M.; Godazgari, S.; Rahdar, A. Development and Evaluation of Azelaic Acid-Loaded Microemulsion for Transfollicular Drug Delivery through Guinea Pig Skin: A Mechanistic Study. *Adv. Pharm. Bull.* 2020, 10, 239.
48. Sivasankarapillai, V.S.; Pillai, A.M.; Rahdar, A.; Sobha, A.P.; Das, S.S.; Mitropoulos, A.C.; Mokarrar, M.H.; Kyzas, G.Z. On facing the SARS-CoV-2 (COVID-19) with combination of nanomaterials and medicine: Possible strategies and first challenges. *Nanomaterials* 2020, 10, 852.
49. Moussavi, S.; Ehrampoush, M.; Mahvi, A.; Rahimi, S.; Ahmadian, M. Efficiency of multi-walled carbon nanotubes in adsorbing humic acid from aqueous solutions. *Asian J. Chem.* 2014, 26, 821.
50. Zhang, J.; Tang, H.; Liu, Z.; Chen, B. Effects of major parameters of nanoparticles on their physical and chemical properties and recent application of nanodrug delivery system in targeted chemotherapy. *Int. J. Nanomed.* 2017, 12, 8483.
51. Zeeshan, M.; Ali, H.; Khan, S.; Khan, S.A.; Weigmann, B. Advances in orally delivered pH-sensitive nanocarrier systems; an optimistic approach for the treatment of inflammatory bowel disease. *Int. J. Pharm.* 2019, 558, 201–214.
52. Barani, M.; Mukhtar, M.; Rahdar, A.; Sargazi, G.; Thysiadou, A.; Kyzas, G.Z. Progress in the Application of Nanoparticles and Graphene as Drug Carriers and on the Diagnosis of Brain Infections. *Molecules* 2021, 26, 186.

53. Wilczewska, A.Z.; Niemirowicz, K.; Markiewicz, K.H.; Car, H. Nanoparticles as drug delivery systems. *Pharmacol. Rep.* 2012, 64, 1020–1037.
54. Moghassemi, S.; Hadjizadeh, A. Nano-niosomes as nanoscale drug delivery systems: An illustrated review. *J. Control. Release* 2014, 185, 22–36.
55. Hamidian, K.; Saberian, M.R.; Miri, A.; Sharifi, F.; Sarani, M. Doped and un-doped cerium oxide nanoparticles: Biosynthesis, characterization, and cytotoxic study. *Ceram. Int.* 2021, 47, 13895–13902.
56. Miri, A.; Najafzadeh, H.; Darroudi, M.; Miri, M.J.; Kouhbanani, M.A.J.; Sarani, M. Iron oxide nanoparticles: Biosynthesis, magnetic behavior, cytotoxic effect. *ChemistryOpen* 2021, 10, 327.
57. Miri, A.; Sarani, M. Biological studies of synthesized silver nanoparticles using Prosopis farcta. *Mol. Biol. Rep.* 2018, 45, 1621–1626.
58. Zhang CY, Xiong D, Sun Y, Zhao B, Lin WJ, Zhang LJ. Self-assembled micelles based on pH-sensitive PAE-g-MPEG-cholesterol block copolymer for anticancer drug delivery. *Int. J. Nanomed.* 2014, 9, 4923-4933.
59. Zhang F, Zhang S, Pollack SF, et al. Improving paclitaxel delivery: in vitro and in vivo characterization of PEGylated polyphosphoester-based nanocarriers. *J. Am. Chem. Soc.* 2015, 137, 2056–2066.
60. Lee MH, Kim EJ, Lee H, et al. Liposomal texaphyrin theranostics for metastatic liver cancer. *J. Am. Chem. Soc.* 2016, 138, 16380–16387.
61. Hu M, Huang P, Wang Y, et al. Synergistic combination chemotherapy of camptothecin and floxuridine through self-assembly of amphiphilic drug-drug conjugate. *Bioconjugate Chem.* 2015, 26, 2497–2506.
62. Tan X, Li BB, Lu X, et al. Light-triggered, self-immolative nucleic Acid-drug nanostructures. *J. Am. Chem. Soc.* 2015, 137, 6112–6115.
63. Farokhzad OC, Langer R. Impact of nanotechnology on drug delivery. *ACS Nano* 2008, 3, 16–20.
64. Quan, Xuebo, Daohui Zhao, Libo Li, and Jian Zhou. Understanding the cellular uptake of pH-responsive zwitterionic gold nanoparticles: a computer simulation study. *Langmuir* 2017, 33, 14480-14489.

65. Mosquera, Jesús, Isabel García, and Luis M. Liz-Marzán. Cellular uptake of nanoparticles versus small molecules: a matter of size. *Acc. Chem. Res.* 2018, 51, 2305-2313.
66. Behzadi, Shahed, Vahid Serpooshan, Wei Tao, Majd A. Hamaly, Mahmoud Y. Alkawareek, Erik C. Dreaden, Dennis Brown, Alaaldin M. Alkilany, Omid C. Farokhzad, and Morteza Mahmoudi. Cellular uptake of nanoparticles: journey inside the cell. *Chem. Soc. Rev.* 2017, 46, 4218-4244.
67. Ramezanpour, M., S. S. W. Leung, K. H. Delgado-Magnero, B. Y. M. Bashe, J. Thewalt, and D. P. Tieleman. Computational and experimental approaches for investigating nanoparticle-based drug delivery systems. *Biochim. Biophys. Acta - Biomembr.* 2016, 1858, 1688-1709.
68. Gajewicz, Agnieszka, Bakhtiyor Rasulev, Tandabany C. Dinadayalane, Piotr Urbaszek, Tomasz Puzyn, Danuta Leszczynska, and Jerzy Leszczynski. Advancing risk assessment of engineered nanomaterials: Application of computational approaches. *Adv. Drug Deliv. Rev.* 2012, 64, 1663-1693.
69. Charbgoo, Fahimeh, Mojgan Nejabat, Khalil Abnous, Fatemeh Soltani, Seyed Mohammad Taghdisi, Mona Alibolandi, W. Thomas Shier, Terry WJ Steele, and Mohammad Ramezani. Gold nanoparticle should understand protein corona for being a clinical nanomaterial. *J. Control. Release.* 2018, 272, 39-53.
70. Payne, Christine K. A protein corona primer for physical chemists. C*hem. Phys*. 2019, 151, 130901.
71. (a) Gliga, A.; Skoglund, S.; Odnevall Wallinder, I.; Fadeel, B.; Karlsson, H. Part. *Fibre Toxicol.* 2014, 11, 11. (b) Limbach, L. K.; Li, Y.; Grass, R. N.; Brunner, T. J.; Hintermann, M. A.; Muller, M.; Gunther, D.; Stark, W. *J. Environ. Sci. Technol.* 2005, 39, 9370−9376. (c) Jiang, J.; Oberdörster, G.; Biswas, P. *J. Nanopart. Res.* 2009, 11, 77−89.
72. Vroman, L., A. L. Adams, G. C. Fischer, and P. C. Munoz. Interaction of high molecular weight kininogen, factor XII, and fibrinogen in plasma at interfaces. *Blood.* 1980, 55, 156-159.
73. Cho, W.-S., Duffin, R., Thielbeer, F., Bradley, M., Megson, I.L., MacNee, W., Poland, C.A., Tran, C.L., Donaldson, K. Zeta potential and solubility to toxic ions

as mechanisms of lung inflammation caused by metal/metal oxide nanoparticles. *Toxicol. Sci.* 2012, 126, 469–477.

74. Clogston, Jeffrey D., and Anil K. Patri. Zeta potential measurement. Characterization of nanoparticles intended for drug delivery. *Humana press.* 2011. 63-70.
75. (a). Mikolajczyk, Alicja, et al. Zeta potential for metal oxide nanoparticles: a predictive model developed by a nano-quantitative structure property relationship approach. *Chem. Mater.* 2020, 27, 2400-2407. (b). Wyrzykowska, Ewelina, et al. Development of a novel in silico model of zeta potential for metal oxide nanoparticles: a nano-QSPR approach. *Nanotechnology.* 2016, 27, 445702.
76. Park, Sung Jean. Protein–nanoparticle interaction: corona formation and conformational changes in proteins on nanoparticles. *Internat. J. Nanomed.* 2020, 15, 5783.
77. Maharjan, Romi Singh, Ajay Vikram Singh, Javaria Hanif, Daniel Rosenkranz, Rashad Haidar, Amruta Shelar, Shubham Pratap Singh et al. Investigation of the Associations between a Nanomaterial's Microrheology and Toxicology. *ACS Omega*. 2022.
78. Cyanide in Biology; Vennesland, B., Comm, E. F., Knownles, J., Westly, J., Wissing, F., Eds.; Academic: London. 1981.
79. P. Gholamzadeh, G.M. Ziarani, N. Lashgari, A. Badiei, A. Shayesteh, M. Jafari, A simple colorimetric chemosensor for naked eye detection of cyanide ion. *J. Fluoresc.* 2016, 26, 1857–1864.
80. Y. Li, H. Zhou, W. Chen, G. Sun, L. Sun, J. Su. A simple AIE-based chemosensor for highly sensitive and selective detection of Hg2+ and CN^-, *Tetrahedron* 2016, 72 5620–5625.
81. A.D.S. Schramm, R. Menger, V.G. Machado. Malononitrile–derivative chromogenic devices for the detection of cyanide in water, *J. Mol. Liq.* 2016, 223, 811–818.
82. Y. Li, J. Chen, T.-S. Chu. Sensing mechanism for a fluorescent off–on chemosensor for cyanide anion. *J. Lumin.* 2016, 179, 203–210.
83. X. Ou, Y. Jin, X. Chen, C. Gong, X. Ma, Y. Wang, C. Chow and Q. Tang. *Anal. Methods.* 2015, 7, 5239–5244.

84. Hijji, Yousef Mohammad, Hani Darwish Tabba, Rajeesha Rajan, Hamzeh Mohammad Abdel-Halim, Musa Ibrahim El-Barghouthi, and Hutaf Mustafa Baker. Selective colorimetric molecular probe for cyanide ion detection in aqueous solution. *European J. Chem.* 2018, 9, 338-346.
85. M. Formica, V. Fusi, L. Giorgi and M. Micheloni. *Coord. Chem. Rev.* 2012, 256, 170–192.
86. L. Chen, D. Wu and J. Yoon. Recent advances in the development of chromophore-based chemosensors for nerve agents and phosgene. *ACS Sens.* 2018, 3, 27–43.
87. Y. Ding, W. H. Zhu and Y. Xie. Development of ion chemosensors based on porphyrin analogues. *Chem. Rev.* 2017, 117, 2203–2256.
88. D. Cao, Z. Liu, P. Verwilst, S. Koo, P. Jangjili, J. S. Kim and W. Lin. Coumarin-based small-molecule fluorescent chemosensors. *Chem. Rev.* 2019, 119, 10403–10519.
89. (a) Martínez-Manez, R.; Sancenon, F. New advances in fluorogenic anion chemosensors. *J. Fluoresc.* 2005, 15, 267-285. (b) Gale, P. A., Ed. Special issue: 35 years of Synthetic Anion Receptor Chemistry. *Coord. Chem. Rev.* 2003, 240. (c) Bondy, C. R.; Loeb, S. J. Amide based receptors for anions. *Coord. Chem. Rev.* 2003, 240, 77. (d) Martínez-Manez, R.; Sancenon, F. Fluorogenic and chromogenic chemosensors and reagents for anions. *Chem. Rev.* 2003, 103, 4419-4476. (e) Suksai, C.; Tuntulani, T. Chromogenic anion sensors. *Chem. Soc. Rev.* 2003, 32, 192. (f) Beer, P. D.; Gale, P. A. Anion recognition and sensing: the state of the art and future perspectives. *Angew. Chem., Int. Ed.* 2001, 40, 486.
90. L. Y. Lin, Y. H. Chen, Z. Y. Huang, H. W. Lin, S. H. Chou, F. Lin, C. W. Chen, Y. H. Liu, K. T. Wong. A low-energy-gap organic dye for high-performance small-molecule organic solar cells. *J. Am. Chem. Soc.* 2011, 133, 15822.
91. Curtarolo S, Hart G L W, Nardelli M B, Mingo N, Sanvito S and Levy O. The high-throughput highway to computational materials design. *Nat. Mater.* 2013, 12, 191–201.
92. Jain A, Shin Y and Persson K A. Computational predictions of energy materials using density functional theory. *Nat. Rev. Mater*. 2016, 1, 15004.
93. Marques MAL, Gross EKU. Time-dependent density functional theory. *Annu. Rev. Phys. Chem*. 2004, 55, 427–455.

94. Cohen AJ, Mori-Sánchez P, Yang W. Insights into current limitations of density functional theory. *Science* 2008, 321, 792–794.
95. Alonso, H.; Bliznyuk, A. A.; Gready, J. E. Combing Docking and Molecular Dynamic Simulations in Drug Design. *Med. Res. Rev.* 2006, 26, 531−568.
96. Ylilauri, M.; Pentikáinen, O. T. MMGBSA as a Tool to Understand the Binding Affinities of Filamin Peptide Interactions. *J. Chem. Inf. Model*. 2013, 53, 2626−2633.
97. Holland John, H. Adaptation in natural and artificial systems. Ann Arbor: University of Michigan Press. 1975.
98. Berrones-Reyes, J.C.; Muñoz-Flores, B.M.; Cantón-Diáz, A.M.; Treto-Suárez, M.A.; Páez-Hernández, D.; Schott, E.; Zarate, X.; Jiménez-Pérez, V.M. Quantum chemical elucidation of the turn-on luminescence mechanism in two new Schiff bases as selective chemosensors of Zn^{2+}: Synthesis, theory and bioimaging applications. *RSC Adv.* 2019, 9, 30778–30789.
99. Wang, X.; Ding, G.; Duan, Y.; Zhu, Y.; Zhu, G.; Wang, M.; Li, X.; Zhang, Y.; Qin, X.; Hung, C.H. A novel triphenylamine-based bis-Schiff bases fluorophores with AIE-Activity as the hydrazine fluorescence turn-off probes and cell imaging in live cells. *Talanta* 2020, 217, 121029.
100. Matsumoto, Y.; Sawamura, J.; Murata, Y.; Nishikata, T.; Yazaki, R.; Ohshima, T. Amino acid schiff base bearing benzophenone imine as a platform for highly congested unnatural α-amino acid synthesis. *J. Am. Chem. Soc.* 2020, 142, 8498–8505.
101. Kontham, V.; Ansari, K.R.; Padmaja, K.V. Tribological properties of 10-undecenoic acid-derived schiff base lubricant additives. *Arab. J. Sci. Eng.* 2021, 46, 5593–5603.
102. Kontham, V.; Ansari, K.R.; Padmaja, K.V.; Madhu, D. Synthesis and evaluation of stearic acid based heterocyclic Schiff bases as biolubricant additives in epoxy karanja fatty acid 2-ethyl hexyl esters base oil. *Industr. Crops Prod.* 2021, 159, 113061.
103. Murmu, M.; Sengupta, S.; Pal, R.; Mandal, S.; Murmu, N.C.; Banerjee, P. Efficient tribological properties of azomethine-functionalized chitosan as a bio-lubricant

additive in paraffin oil: Experimental and theoretical analysis. *RSC Adv.* 2020, 10, 33401–33416.

104. Kumar, B.; Kuntail, J.; Verma, D.K.; Rastogi, R.B.; Sinha, I. Mechanism of triboactivity of Schiff bases: Experimental and molecular dynamics simulations studies. *J. Mol. Liq.* 2019, 289, 111171.
105. Maity, D. Recent studies on applications of Schiff bases and their complexes in atmospheric carbon dioxide capture. *Russ. J. Gen. Chem.* 2020, 90, 2473–2483.
106. Xing, H.; Yaylayan, V. Mechanochemical generation of Schiff bases and Amadori products and utilization of diagnostic MS/MS fragmentation patterns in negative ionization mode for their analysis. *Carbohydr. Res.* 2020, 495, 108091.
107. Alamro, F.S.; Gomha, S.M.; Shaban, M.; Altowyan, A.S.; Abolibda, T.Z.; Ahmed, H.A. Optical investigations and photoactive solar energy applications of new synthesized Schiff base liquid crystal derivatives. *Sci. Rep.* 2021, 11, 1–11.
108. Gomha, S.M.; Ahmed, H.A.; Shaban, M.; Abolibda, T.Z.; Khushaim, M.S.; Alharbi, K.A. Synthesis, optical characterizations and solar energy applications of new Schiff base materials. *Materials.* 2021, 14, 3718.
109. Jiang, L.; Tian, Y.; Cheng, J.; Zhang, J. A biomass-based Schiff base vitrimer with both excellent performance and multiple degradability. *Polym. Chem.* 2021, 12, 6527–6537.
110. Patra, Jayanta Kumar, Gitishree Das, Leonardo Fernandes Fraceto, Estefania Vangelie Ramos Campos, Maria del Pilar Rodriguez-Torres, Laura Susana Acosta-Torres, Luis Armando Diaz-Torres et al. Nano based drug delivery systems: recent developments and future prospects. *J. Nanobiotechnology* 2018, 16, 1-33.
111. Zhang, Lei, WF Drew Bennett, Tao Zheng, Ping-Kai Ouyang, Xinping Ouyang, Xueqing Qiu, Anqi Luo, Mikko Karttunen, and P. Chen. Effect of cholesterol on cellular uptake of cancer drugs pirarubicin and ellipticine. *J. Phys. Chem. B* 120. 2016, 12, 3148-3156.
112. Zhang, Xiao, Guanghui Ma, and Wei Wei. Simulation of nanoparticles interacting with a cell membrane: probing the structural basis and potential biomedical application. *NPG Asia Materials*, 2021, 13, 52.
113. Sizochenko, Natalia, Alicja Mikolajczyk, Michael Syzochenko, Tomasz Puzyn, and Jerzy Leszczynski. Zeta potentials (ζ) of metal oxide nanoparticles: A meta-analysis

of experimental data and a predictive neural networks modeling. *NanoImpact*, 2021, *22,* 100317.

114. Kumari, Namita, Satadru Jha, and Santanu Bhattacharya. An Efficient Probe for Rapid Detection of Cyanide in Water at Parts per Billion Levels and Naked-Eye Detection of Endogenous Cyanide. *Chem. Asian J.* 2014, 9, 830-837.
115. Low, May Lee, Laure Maigre, Pierre Dorlet, Regis Guillot, Jean-Marie Pages, Karen A. Crouse, Clotilde Policar, and Nicolas Delsuc. Conjugation of a new series of dithiocarbazate Schiff base copper (II) complexes with vectors selected to enhance antibacterial activity. *Bioconjug. Chem.* 2014, 25, 2269-2284.
116. Hanwell, M. D.; Curtis, D. E.; Lonie, D. C.; Vandermeersch, T.; Zurek, E.; Hutchison, G. Avogadro: an advanced semantic chemical editor, visualization, and analysis platform. *J. Cheminformatics.* 2012, 4, 17.
117. Frisch MJ, Trucks JW, Schlegel HB, Scuseria G, Robb MA, Cheeseman JR, et al. Gaussian 09, revision B.01. 2009.
118. Fuhrmann, J.; Rurainski, A.; Lenhof, H.-P.; Neumann, D. A new Lamarckian genetic algorithm for flexible ligand-receptor docking. *J. Comput. Chem.* 2010, 31, 1911−1918.
119. Magar, R.; Yadav, P.; Barati Farimani, A. Potential neutralizing antibodies discovered for novel corona virus using machine learning. *Sci. Rep.* 2021, 11, 5261.
120. Hess, B.; Kutzner, C.; van der Spoel, D.; Lindahl, E. GROMACS 4: algorithms for highly efficient, load-balanced, and scalable molecular simulation. *J. Chem. Theory Comput.* 2008, 4, 435− 447.
121. Ryckaert, J.-P.; Ciccotti, G.; Berendsen, H. Numerical integration of the cartesian equations of motion of a system with constraints: molecular dynamics of n-alkanes. *J. Comput. Phys.* 1977, 23, 327−341.
122. Miyamoto, S.; Kollman, P. A. Settle: An analytical version of the SHAKE and RATTLE algorithm for rigid water models. *J. Comput. Chem.* 1992, 13, 952−962.
123. Kumari, R.; Kumar, R.; Lynn, A.; Open-Source Drug Discovery Consortium. G_mmpbsa - A GROMACS tool for high-throughput MM-PBSA calculations. *J. Chem. Inf. Model.* 2014, 54, 1951−1962.

124. Vorontsov, I. I.; Miyashita, O. Crystal molecular dynamics simulations to speed up MM/PB (GB) SA evaluation of binding free energies of di-mannose deoxy analogs with P51G-m4-Cyanovirin-N. *J. Comput. Chem.* 2011, 32, 1043−1053.
125. Sa, R.; Fang, L.; Huang, M; Li, Q.; Wei, Y.; Wu, K. Evaluation of interactions between urokinase plasminogen and inhibitors using molecular dynamic simulation and free-energy calculation. *J. Phys. Chem. A*. 2014, 118, 9113−9119.
126. Hornak, V.; Abel, R.; Okur, A.; Strockbine, B.; Roitberg, A.; Simmerling, C. Comparison of multiple Amber force fields and development of improved protein backbone parameters. *Proteins.* 2006, 65, 712−725.
127. Homeyer, N.; Gohlke, H. Free energy calculations by the molecular mechanics Poisson- Boltzmann surface area method. *Mol. Inform*. 2012, 31, 114−122.
128. Pal, T. K.; Mumit, M. A.; Hossen, J.; Paul, S.; Alam, M. A.; Islam, M. A.-A.-A.-A.; Sheikh, M. C. Computational and experimental insight into antituberculosis agent, (E)-benzyl-2-(4-hydroxy-2-methoxybenzylidene) hydrazinecarbodithioate: ADME analysis. *Heliyon*. 2021, 7, e08209.
129. Sengottiyan, Selvaraj, Kakoli Malakar, Arunkumar Kathiravan, Marappan Velusamy, Alicja Mikolajczyk, and Tomasz Puzyn. Integrated Approach to Interaction Studies of Pyrene Derivatives with Bovine Serum Albumin: Insights from Theory and Experiment. *J. Phys. Chem. B.* 2022, 126, 3831−3843.
130. Ropp, Patrick J., Jesse C. Kaminsky, Sara Yablonski, and Jacob D. Durrant. Dimorphite-DL: an open-source program for enumerating the ionization states of drug-like small molecules. *J. Cheminform.* 2019, 11, 1-8.
131. S. Jo, T. Kim, V.G. Iyer, W. Im, CHARMM-GUI: A web-based graphical user interface for CHARMM. *J. Comput. Chem.* 2008, 29, 1859–1865.
132. R.M. Venable, A.J. Sodt, B. Rogaski, H. Rui, E. Hatcher, A.D. MacKerell, R.W. Pastor, J.B. Klauda. CHARMM all-atom additive force field for sphingomyelin: Elucidation of hydrogen bonding and of positive curvature. *Biophys. J.* 2014, 107, 134–145.
133. Jorgensen, W. L., Chandrasekhar, J., Madura, J. D., Impey, R. W. & Klein, M. L. Comparison of simple potential functions for simulating liquid water. *J. Chem. Phys.* 1983, 79, 926–935.

134. Thallmair, Sebastian, Matti Javanainen, Balázs Fábián, Hector Martinez-Seara, and Siewert J. Marrink. Nonconverged Constraints Cause Artificial Temperature Gradients in Lipid Bilayer Simulations. *J. Phys. Chem. B.* 2021, 125, 9537-9546.
135. Case, D.A. et al. The Amber biomolecular simulation programs. *J. Comput. Chem.* 2005, 26, 1668–1688.
136. J.P. Ryckaert, G. Ciccotti, H.J.C. Berendsen. Numerical integration of the cartesian equations of motion of a system with constraints: molecular dynamics of n-alkanes, *J. Comput. Phys.* 1977, 23, 327–341.
137. Hess, Berk, Carsten Kutzner, David Van Der Spoel, and Erik Lindahl. GROMACS 4: algorithms for highly efficient, load-balanced, and scalable molecular simulation. *J. Chem. Theory. Comput.* 2008, 4, 435-447.
138. Chodera, J. D., Swope, W. C., Pitera, J. W., Seok, C. & Dill, K. A. Use of the weighted histogram analysis method for the analysis of simulated and parallel tempering simulations. *J. Chem. Theory Comput.* 2007, 3, 26–41.
139. Zhao, Yating, Yu Wang, Fu Ran, Yu Cui, Chang Liu, Qinfu Zhao, Yikun Gao, Da Wang, and Siling Wang. A comparison between sphere and rod nanoparticles regarding their in vivo biological behavior and pharmacokinetics. *Sci. Rep.* 2017, 7, 1-11.
140. Ma, Liang, Chao Wang, Zihao He, Biao Cheng, Ling Zheng, and Kun Huang. Peptide-drug conjugate: a novel drug design approach. *Curr. Med. Chem.* 2017, 24, 3373-3396.
141. Selvaraj Sengottiyan, Alicja Mikolajczyk, Tomasz Puzyn. How does the study MD of pH-dependent exposure of nanoparticles affect cellular uptake of anticancer drugs? *Int. J. Mol. Sci.* 2023,
142. Tieleman, D. Peter, Lucy R. Forrest, Mark SP Sansom, and Herman JC Berendsen. Lipid properties and the orientation of aromatic residues in OmpF, influenza M2, and alamethicin systems: molecular dynamics simulations. *Biochemistry.* 1998, 37, 17554-17561.
143. Hyslop, Paul A., Benoit Morel, and Richard D. Sauerheber. Organization and interaction of cholesterol and phosphatidylcholine in model bilayer membranes. *Biochemistry* 1990, 29, 1025-1038.

144. Pabst, Georg, Michael Rappolt, Heinz Amenitsch, and Peter Laggner. Structural information from multilamellar liposomes at full hydration: full q-range fitting with high quality x-ray data. *Phys. Rev. E.* 2000, 62, 4000.
145. Mizuhara, Tsukasa, Krishnendu Saha, Daniel F. Moyano, Chang Soo Kim, Bo Yan, Young-Kwan Kim, and Vincent M. Rotello. Acylsulfonamide-functionalized Zwitterionic gold nanoparticles for enhanced cellular uptake at tumor pH. *Angew. Chem., Int. Ed.* 2015, 127, 6667-6670.
146. Kučerka, N., Tristram-Nagle, S. & Nagle, J. F. Structure of fully hydrated fluid phase lipid bilayers with monounsaturated chains. *J. Membr. Biol.* 2006, 208, 193–202.
147. Marrink, Siewert-Jan, and Herman JC Berendsen. Simulation of water transport through a lipid membrane. *J. Phys. Chem.* 1994, 98, 4155-4168.
148. Toroz, D., and I. R. Gould. A computational study of Anthracyclines interacting with lipid bilayers: Correlation of membrane insertion rates, orientation effects and localisation with cytotoxicity. *Sci. Rep.* 2019, 9, 1-12.
149. Berrecoso, Germán, José Crecente-Campo, and María José Alonso. Unveiling the pitfalls of the protein corona of polymeric drug nanocarriers. *Drug Deliv. Transl. Res.* 2020, 10, 730-750.
150. Schaftenaar, Gijs, and Jan H. Noordik. Molden: a pre-and post-processing program for molecular and electronic structures. *J. Comput. Aided. Mol. Des.* 2000, 14, 123-134.
151. Todeschini, Roberto, Marina Lasagni, and Emilio Marengo. New molecular descriptors for 2D and 3D structures. Theory. *J. Chemom.* 1994, 8, 263-272.
152. Gramatica, Paola, Pamela Pilutti, and Ester Papa. Validated QSAR prediction of OH tropospheric degradation of VOCs: splitting into training - test sets and consensus modeling. *J. Chem. Inf. Comput. Sci.* 2004, 44, 1794-1802.
153. Gramatica, Paola. Principles of QSAR models validation: internal and external. *QSAR Comb. Sci.* 2007, 26, 694-701.
154. Cronin, Mark TD, ed. Predicting chemical toxicity and fate. CRC press. 2004.
155. Cronin, Mark TD, and T. Wayne Schultz. Pitfalls in QSAR. *J. Mol. Struct. THEOCHEM.* 2003, 622, 39-51.

156. Holland John, H. Adaptation in natural and artificial systems. Ann Arbor: University of Michigan Press. 1975.
157. Wold, Herman. Soft modeling: the basic design and some extensions. Systems under indirect observation. Causality. Structure. Prediction. Ed. KG Joreskog. H. Wold. Amsterdam: North Holland Publishing Company, 1982.
158. Wold, Svante, Arnold Ruhe, Herman Wold, and W. J. Dunn, Iii. The collinearity problem in linear regression. The partial least squares (PLS) approach to generalized inverses. *SIAM J Sci Comput*. 1984, 5, 735-743.
159. Wold, Svante, Michael Sjöström, and Lennart Eriksson. PLS-regression: a basic tool of chemometrics. *Chemom. Intell. Lab. Syst.* 2001, 58, 109-130.
160. Cawley, Gavin C., and Nicola LC Talbot. Efficient approximate leave-one-out cross-validation for kernel logistic regression. *Mach. Learn.* 2008, 71, 243-264.
161. Tekie, Farnaz Sadat Mirzazadeh, Maliheh Hajiramezanali, Parham Geramifar, Mohammad Raoufi, Rassoul Dinarvand, Masoud Soleimani, and Fatemeh Atyabi. Controlling evolution of protein corona: A prosperous approach to improve chitosan-based nanoparticle biodistribution and half-life. *Sci. Rep.* 2020, 10, 1-14.
162. Papadiamantis, Anastasios G., et al. Computational enrichment of physicochemical data for the development of a ζ-potential read-across predictive model with Isalos Analytics Platform. *NanoImpact*. 2021, 22, 100308.
163. Gibson, N.; Shenderova, O.; Luo, T. J. M.; Moseenkov, S.; Bondar, V.; Puzyr, A.; Purtov, K.; Fitzgerald, Z.; Brenner, D. W. *Diam. Relat. Mater.* 2009, 18, 620−626.
164. Cedervall, Tommy, Iseult Lynch, Martina Foy, Tord Berggård, Seamas C. Donnelly, Gerard Cagney, Sara Linse, and Kenneth A. Dawson. Detailed identification of plasma proteins adsorbed on copolymer nanoparticles. *Angew. Chem. Int. Ed.* 2007, 46, 5754-5756.
165. Cho, Wan-Seob, Frank Thielbeer, Rodger Duffin, Emma MV Johansson, Ian L. Megson, William MacNee, Mark Bradley, and Ken Donaldson. Surface functionalization affects the zeta potential, coronal stability and membranolytic activity of polymeric nanoparticles. *Nanotoxicology.* 2014, 8, 202-211.
166. Somarathne, Radha P., Emily R. Chappell, Y. Randika Perera, Rahul Yadav, Joo Youn Park, and Nicholas C. Fitzkee. Understanding how staphylococcal autolysin domains interact with polystyrene surfaces. *Front. Microbiol.* 2021, 12, 1146.

167. Patil, Swanand, Amanda Sandberg, Eric Heckert, William Self, and Sudipta Seal. Protein adsorption and cellular uptake of cerium oxide nanoparticles as a function of zeta potential. *Biomaterials.* 2007, 28, 4600-4607.

168. (a). Murugappan, Gunavadhi, and Kalarical Janardhanan Sreeram. Nano-biocatalyst: Bi-functionalization of protease and amylase on copper oxide nanoparticles. *Colloids. Surf. B: Biointerfaces.* 2021, 197, 111386. (b). Vroman, Leo, et al. Interaction of high molecular weight kininogen, factor XII, and fibrinogen in plasma at interfaces. *Blood.* 1980, 156-159. (c). Vroman, L., and A. N. N. Lukosevicius. Ellipsometer recordings of changes in optical thickness of adsorbed films associated with surface activation of blood clotting. *Nature.* 1964, 204, 701-703. (d). Cho, Wan-Seob, et al. Surface functionalization affects the zeta potential, coronal stability and membranolytic activity of polymeric nanoparticles. *Nanotoxicology.* 2014, 8, 202-211.

169. Thielbeer, Frank, Ken Donaldson, and Mark Bradley. Zeta potential mediated reaction monitoring on nano and microparticles. *Bioconjug. Chem*. 2011, 22, 144-150.

170. Sakulkhu, Usawadee, et al. Protein corona composition of superparamagnetic iron oxide nanoparticles with various physico-chemical properties and coatings. *Sci. Rep.* 2014, 4, 1-9.

171. Hirsch, Vera, Calum Kinnear, Marc Moniatte, Barbara Rothen-Rutishauser, Martin JD Clift, and Alke Fink. Surface charge of polymer coated SPIONs influences the serum protein adsorption, colloidal stability and subsequent cell interaction in vitro. *Nanoscale.* 2013, 5, 3723-3732.

172. Hasegawa, K., and K. Funatsu. Partial least squares modeling and genetic algorithm optimization in quantitative structure-activity relationships. *SAR QSAR Environ Res.* 2000, 11, 189-209.

173. Yallapu, Murali M., et al. Implications of protein corona on physico-chemical and biological properties of magnetic nanoparticles. *Biomaterials.* 2015, 46, 1-12.

174. Singh, Ajay Vikram, Yunus Alapan, Timotheus Jahnke, Peter Laux, Andreas Luch, Amirreza Aghakhani, Soheila Kharratian, Mehmet Cengiz Onbasli, Joachim Bill, and Metin Sitti. Seed-mediated synthesis of plasmonic gold nanoribbons using cancer cells for hyperthermia applications. *J. Mater. Chem. B.* 2018, 6, 7573-7581.

175. Kathiravan, Arunkumar, Selvaraj Sengottiyan, Tomasz Puzyn, Pushparathinam Gopinath, Kanagachidambaresan Ramasubramanian, Praveen Ayyappan Susila, and Mariadoss Asha Jhonsi. Rapid colorimetric discrimination of cyanide ions–mechanistic insights and applications. *Analytical Methods.* 2022, 14, 518-525.

ORIGINAL PUBLICATIONS

STATEMENTS